Occurrence frequency of ~~Kelvin Helmholtz instability~~subcritical Richardson number assessed by global high-resolution radiosonde and ERA5 reanalysis

Jia Shao[1]; Jian Zhang[2]*; Wuke Wang[3]; Shaodong Zhang[4]; Tao Yu[2]; Wenjun Dong[5,6]

[1] College of Informatics, Huazhong Agricultural University, Wuhan 430070, China
[2] Hubei Subsurface Multi-scale Imaging Key Laboratory, School of Geophysics and Geomatics, China University of Geosciences, Wuhan 430074, China
[3] School of environmental studies, China University of Geosciences, Wuhan 430074, China
[4] School of Electronic Information, Wuhan University, Wuhan 430072, China
[5] Center for Space and Atmospheric Research (CSAR), Embry-Riddle Aeronautical University, Daytona Beach, FL, USA
[6] Global Atmospheric Technologies and Sciences (GATS), Boulder, CO, USA

Correspondence to:
Dr. Jian Zhang (Email: zhangjian@cug.edu.cn)

Abstract. Kelvin Helmholtz instability (KHI) is most likely to be the primary source for clear-air turbulence that is of importance in pollution transfer and diffusion and aircraft safety. ~~It is exemplarily indicated by the critical value of Richardson (*Ri*) number, which is typically taken as 1/4.~~ It is indicated by the critical value of the dimensionless Richardson (*Ri*) number, which is predicted to be 1/4 from linear stability analysis. However, *Ri* is fairly ~~–~~sensitive to the vertical resolution of the dataset; ~~:~~ a higher resolution systematically leads to a finer structure. The study aims to evaluate the performance of ERA5 reanalysis ~~(137 model levels)~~ in determining the spatial-temporal variabilities of ~~KHI~~ subcritical *Ri*~~spatial-temporal variabilities~~ ~~,~~ by comparing it against a near-global high-resolution ~~(10 m)~~ radiosonde dataset during years 2017 to 2022 ~~,~~ and ~~to~~ further highlight ~~the~~ global climatology and dynamical environment of subcritical *Ri*~~KHIs~~. Overall, the occurrence frequency of $Ri<1/4$ ~~in the free atmosphere~~ is inevitably underestimated by the ERA5 reanalysis over all climate zones at all heights from near-ground up to 30 km, compared to radiosonde, due largely to the severe underestimation in wind shears. Otherwise, the occurrence frequency of ~~of KHI indicated by~~ $Ri<1$ in ERA5 is climatologically consistent with that from $Ri<1/4$ in radiosondes in the free troposphere, especially over the midlatitude and subtropics in the Northern/Southern Hemisphere. Therefore, we ~~infer~~ argue that ~~the~~ threshold value of *Ri* ~~should~~ could be approximated as 1 ~~,~~ rather than 1/4 ~~,~~ when using ERA5-based *Ri* as proxy for KHI ~~for the KHI estimation~~. The occurrence frequency of subcritical *Ri*~~KHI occurrence frequencies~~ revealed by both datasets exhibits significant seasonal cycles over all climate zones ~~polar, midlatitude, and subtropics regions, and they are consistently strong at heights of 10–15 km in the tropic region~~. In addition, ~~the frequency~~it ~~at low-levels~~ is positively correlated with the standard derivation of orography at low-levels ~~,~~ and ~~it~~ is exceptionally strong over the Niño 3 region at heights of 6–13 km. Furthermore, high occurrence of subcritical *Ri* would likely be accompanied by strong wind speeds and intensive orographic or non-orographic gravity waves.

~~Furthermore, the dynamical environment of KHI favors strong wind shears probably induced by the mean flows and the propagation of orographic or non-orographic gravity~~

设置了格式: 字体颜色: 自动设置

设置了格式: 字体颜色: 自动设置

设置了格式: 字体: 倾斜, 字体颜色: 自动设置

设置了格式: 字体颜色: 自动设置

设置了格式: 字体颜色: 自动设置

设置了格式: 字体: 倾斜

设置了格式: 字体: 倾斜

设置了格式: 字体颜色: 自动设置

设置了格式: 字体: 倾斜, 字体颜色: 自动设置

设置了格式: 字体: 非倾斜

waves.

Key words: High-resolution radiosonde dataset; ERA5 reanalysis; Kelvin Helmholtz instabilityWind shears; Threshold Richardson number; Gravity waves

Introduction

Kelvin Helmholtz instability (KHI) is a common phenomenon in the atmospheric boundary layer and the free atmosphere (Muschinski and Wode, 1998), and its wavelengths and depths span a wide range of scales throughout the atmosphere, varying from few meters or less to 10s of km (Fritts et al., 2011). It contributes to vertical mixing of heat, momentum, and constituents, and it acts to limit the maximum shears, just to name a few (Fritts et al., 2011). KHI along with gravity wave (GW) breaking are the most recognized instabilities in stably stratified flows (Fritts and Rastogi, 1985). In addition, GW breaking has been identified as important sources of instability (e.g., Fritts et al., 2020; Dong et al., 2020, 2021, 2022). KHI arises preferentially from micro- and mesoscale wind shear intensificationon strong shears due to medium-frequency and lower frequency GWs, tides, planetary waves (PWs), and mean flows (Baumgarten and Fritts, 2014), with maximal occurrence frequency near synoptic scale upper-level frontal zones near jet streams, with mountain waves, and above the tops of severe thunderstorms (North et al., 2014).. Large wind shear is commonly associated with regions where stability changes rapidly (e.g., near the top of the boundary layer) and the large wind gradient in jet stream (Grasmick and Geerts, 2020). In a changing climate, wind shear in the North Atlantic upper-level jet stream could be increased (Lee et al., 2019), which may increase clear-air turbulence at cruise altitudes. In turn, KHI can reduce wind shears and alter tracer gradients where turbulence and mixing are most intense (Fritts et al., 2022).

带格式的: 段落间距段前: 12 磅

设置了格式: 非突出显示

In addition, complex terrain may locally enhance wind shear, leading to KHI (Grasmick and Geerts, 2020). Large wind shear is common in regions where stability changes rapidly (e.g., near the top of the boundary layer) and the associated large gradient in jet stream (Grasmick and Geerts 2020), which may increase clear air turbulence (Williams and Joshi, 2013). In turn, KHI can reduce wind shears and alter tracer gradients where turbulence and mixing are most intense (Fritts et al., 2022).

KHI influences depend on the spatial scales at which they lead to turbulence (Fritts et al., 2022). Turbulence is by far the most common cause of serious injuries to aircraft (Williams and Joshi, 2013). Convective instability, shear instability, KHI, and GW breaking are known to be the major sources for turbulence (Sharman et al., 2012; Ko et al., 2019; 2022). Among others, KHI is one of the most common causes of turbulence throughout the atmosphere from Earth's surface to the lower thermosphere (Fritts et al., 2011; Sharman et al., 2012). KHI requires a sufficiently large Reynolds number and a Richardson (*Ri*) number sufficiently below 1/4 to enable KHI formation and subsequent secondary instability leading to turbulence (Fritts et al., 2022). *Ri* is not a good guide to instability character in general, and *Ri*>1/4 does not assure flow stability for superpositions of mean and GW motions. Despite these caveats, *Ri*<1/4 does provide a reasonable guide to expected local KHI structure in cases where clear KH billows arise, according to the simulation in the mesosphere and lower thermosphere region (Fritts et al., 2014). Values of *Ri* close to zero favor strong instability, deep billows, and relatively intense turbulence, whereas values of *Ri* closer to 1/4 favor weak instability, shallow billows (Fritts et al., 2011). The Richardson number criterion can be applied as a turbulence diagnostic in numerical model output (e.g. Sharman and Pearson, 2017), and it has been used as such in climatological studies on the occurrence of clear air turbulence (Jaeger and Sprenger, 2007). Kunkel et al. (2019) includes a brief discussion on the capability of ECMWF models based on case studies to resolve subcritical Richardson numbers, and argues that the threshold value of *Ri* (*Rit*) taken as 1 might be a good proxy for observed KHI. A very recent study by Lee at al. (2023) also sets *Rit* from 0–1 in their climatology on the upper troposphere and lower stratosphere turbulence diagnostics. The threshold value of *Ri* can be potentially used an indicator

设置了格式

设置了格式: 字体颜色: 自动设置
设置了格式: 字体颜色: 自动设置
设置了格式: 非突出显示
设置了格式: 字体颜色: 自动设置
设置了格式: 非突出显示
设置了格式: 字体颜色: 自动设置
设置了格式: 字体颜色: 自动设置
设置了格式: 非突出显示
设置了格式: 字体: 倾斜, 非突出显示
设置了格式: 非突出显示
设置了格式: 字体: 非倾斜, 非突出显示
设置了格式: 非突出显示
设置了格式: 字体: 非倾斜, 非突出显示
设置了格式: 非突出显示
设置了格式: 字体: 非倾斜, 非突出显示
设置了格式: 非突出显示
设置了格式: 字体: 非倾斜, 非突出显示
设置了格式: 非突出显示
设置了格式: 字体颜色: 自动设置
设置了格式: 非突出显示
设置了格式: 字体颜色: 自动设置
设置了格式: 非突出显示
设置了格式: 非突出显示
设置了格式: 字体: 非倾斜, 非突出显示
设置了格式: 字体: 非倾斜, 非突出显示
设置了格式: 非突出显示
设置了格式: 字体颜色: 自动设置
设置了格式: 非突出显示
设置了格式: 字体颜色: 自动设置

~~of turbulence (for instance, Jaeger et al., 2007).~~ Moreover, Zhang et al. (2022) shows that over half of turbulence exists below *Ri*<1 when the environment is beneficial for the development of turbulence~~ (Zhang et al., 2022)~~.

Turbulent mixing is of crucial importance to mass, energy, momentum transfer, the dispersion of pollutants, and stratosphere-troposphere exchange. I~~i~~n numerical models, turbulent dissipation rate, turbulent diffusivity and other parameters representing turbulent mixing efficiency are the most basic parameters, which need to be accurately parameterized to evaluate the impact of turbulence~~t~~ effect on matter and energy distribution (Gavrilov et al., 2005). ~~However, it presents a challenge both in observation and numerical modeling (Sharman et al., 2012; Homeyer et al., 2014; Plougonven and Zhang, 2014).~~ However, d~~D~~ue to the intermittent nature of turbulence it is generally not resolved in (global) numerical weather prediction models, even at nowadays common/states of the art horizontal resolutions of the order of tens of kilometers (Sandu et al., 2019)~~,~~ and it presents a challenge both in observation and numerical modeling (Sharman et al., 2012; Homeyer et al., 2014; Plougonven and Zhang, 2014). ~~While in numerical models, turbulent dissipation rate, turbulent diffusivity and other parameters representing turbulent mixing efficiency are the most basic parameters, which need to be accurately parameterized to evaluate the impact of turbulent effect on matter and energy distribution (Gavrilov et al., 2005).~~ For this reason, ~~For this reason,~~ the indices of turbulence, such as large wind shear, small *Ri* and ~~,~~ the negative squared Brunt-väisälä frequency, could be a great tool to characterize turbulence (Jaeger et al., 2007).

The Richardson number ~~*Ri*~~ is estimated by the finite differences across thin layers and is quite sensitive to the vertical resolution of measurements (Haack et al., 2014). Thus, a proper estimation of *Ri* requires a high-resolution measurement of temperature and wind speed. The near-global distributed radiosonde site offers a unique opportunity to investigate the climatology of subcritical *Ri* ~~KHI~~ occurrence frequency. The overview of subcritical *Ri* ~~KHI~~ occurrence by using a near-global high-resolution (10-m) radiosonde data was presented in Zhang et al. (2022), and a close association between subcritical *Ri* ~~KHI~~ occurrence frequency and turbulence fraction has been

设置了格式: 字体颜色: 自动设置

设置了格式: 字体: 倾斜

found. However, the global climatology characteristic of subcritical *Ri* ~~KHI~~ remains most unclear, especially over oceans where the radiosonde network has a poor coverage.

By comparison, ERA5 global reanalysis can provide a seamless coverage of temperature and wind, and it is the last version of the European Centre for Medium-Range Weather Forecasts (ECMWF) model and has 137 model levels (Hersbach et al., 2020). ~~It experiences a lot of improvements, including the statistically significant improvement in short-range forecasts by the Aeolus satellite (Rennie et al., 2021).~~ Its predecessor, ERA-Intrim, was found in particular wind shear a factor of 2–3 lower simulated based on high-resolution radiosondes (Houchi et al., 2010). Moreover, results show that whatever the location and the geophysical conditions considered, biases between ERA-Interim and balloon wind measurements increase as a function of altitude (Duruisseau et al., 2017). Recent studies have suggested that the structure and variability of the trade winds in the lower troposphere are reasonably reproduced in the ERA5 reanalysis based on the EUREC4A field campaign (Savazzi et al., 2022). However, the similar comparison between ERA5 and high-resolution radiosonde across a near-global area has largely been undetermined. The proper estimation of wind shear and Brunt-Väisälä frequency is essential for the determination of *Ri*.

Thus, our objectives are to: (1) Evaluate the performance of ERA5 at different heights and climate zones in estimating wind shear and small Richardson number occurrence frequencies, in comparison with a large high-resolution radiosonde dataset spanning the years from 2017 to 2022~~Thus, our objectives are to: (1) The performance of ERA5 (137 model levels) at different heights and climate zones in estimating wind shear and KHI occurrence frequency, comparing with a large high resolution (10 m) radiosonde dataset spanning years from 2017 to 2022~~. (2) Based on the validation and comparison results, we pose a question: how to use ERA5 for ~~KHI~~ subcritical *Ri* ~~study~~estimation? (3) The global climatology of ~~KHI~~ subcritical *Ri* occurrence based on versatile measurements and model products. (4) The dynamic environment (GWs and mean flow) of subcritical *Ri*~~KHI~~. These works would be valuable for the understanding of the global distribution of subcritical *Ri*~~KHI~~, and furthermore, turbulence fraction. To this end, this analysis is organized as follows. Section 2 shows the data and methods

设置了格式: 字体: 倾斜

设置了格式: 字体: 倾斜

used. Section 3 represents the climatological variation of subcritical *Ri* ~~KHI~~ and its comparison with radiosonde. Section 4 ends with a summary.

2 Data and methods

2.1 High-resolution radiosonde dataset

As described in Guo et al. (2021) and Zhang et al. (2022), a high vertical resolution radiosonde (HVRRS) dataset gained from several organizations was adopted, spanning January 2017 to October 2022, in a total of 5.8 years. The organizations include the China Meteorological Administration (CMA), the U.S National Oceanic and Atmospheric Administration (NOAA), the Global Climate Observing System (GCOS) Reference Upper-Air Network (GRUAN), the Centre for Environmental Data Analysis of the United Kingdom (CEDA), University of Wyoming, Deutscher Wetterdienst, and ECMWF. In total, around 0.95~~115~~ million radiosonde profiles from 434 radiosonde stations released at regular synoptic times of 0000 UTC and 1200 UTC were collected to determine the value of *Ri*. These profiles were sampled at 0.5 Hz or 1 Hz, corresponding to a vertical resolution of approximately 10 m or 5 m. Thus, all the profiles were evenly interpreted to 10 m resolution in vertical by applying a cubic spline interpolation. In addition, the sounding with the burst height lower than 10 km above ground level (a.g.l.) was directly discarded for further study. Meteorological variables, including temperature and wind speed, were prepared for the *Ri* estimation.

One of the ~~shortage~~shortages of radiosonde measurements is its inadequate concentration over the polar and ocean regions (Xia et al., 2021). The geographical distribution of total profile number of each radiosonde station is demonstrated in Figure S1 in the supporting information~~in Support Information~~. The released radiosoundings over Europe, the United States, and Australia have good geographical coverage and time duration. Over some islands of oceans (e.g., the Pacific Ocean) there are dozens of stations that can provide high-resolution measurement. Over the polar regions, there

设置了格式: 字体颜色: 自动设置

设置了格式: 字体颜色: 自动设置

are around thirty stations.

2.2 ERA5 reanalysis and the collocation procedure

ERA5 is the latest version of ECMWF meteorological reanalysis, benefiting from a decade of developments in model physics, core dynamics, and data assimilation (Hersbach et al., 2020). The wind and temperature fields are modelled by the ERA5 reanalysis on a spatial resolution of 0.25° latitude/longitude and a temporal resolution of 1 hour. The reanalysis has 137 model levels, giving a vertical resolution of approximately 300 m in the middle and upper troposphere and 500 m in the lower stratosphere. The vertical resolution of ERA5 is illustrated in Figure S2. Compared to ERA5, the HVRRS does not provide global seamless observations Compared to ERA5 reanalysis, the HVRRS is hard to provide global seamless observations. Thus, the collocation procedure between reanalysis and HVRRS goes as follows: (1) the matched grid of ERA5 reanalysis is the nearest neighbor of radiosonde station; (2) the regular synoptic start time of radiosonde and reanalysis needs to keep exact the same; (3) the pressure coordinate of reanalysis is converted into geometric altitude to match with HVRRS.

In addition, the standard deviations of orography (SDOR) and the gravity wave dissipation due to the effects of stress associated with unresolved valleys, hills and mountains and near-surface wind speed at 10 m in ERA5 reanalysis are extracted.

The relative error between HVRRS-based and ERA5-based quantities is estimated by the ratio of deviations between HVRRS and ERA5 derived quantities to the HVRRS one.

2.3 The occurrence frequency of subcritical *Ri*KHI and its uncertainty

The burst of KHI is characterized by the occurrence of the *Ri* under a critical value which is frequently taken as 1/4, and

Based on a linear theory, the threshold *Ri* (*Rit*) defines the threshold where the air

设置了格式: 字体颜色: 自动设置

设置了格式: 字体颜色: 自动设置

带格式的: 缩进: 首行缩进: 0.74 厘米

设置了格式

设置了格式: 字体: 倾斜

带格式的: 标题 2, 缩进: 首行缩进: 0 厘米, 行距: 单倍行距

设置了格式: 字体: 倾斜

设置了格式: 字体: 倾斜

flow changes from stability to turbulence, and it is usually suggested to be 1/4 (Haack et al., 2014). *Ri* is formulated as:

Ri is formulated as:

$$\mathrm{Ri} = \bar{N}^2/\bar{S}^2 \qquad (1)$$

where N is the Brunt-Väisälä frequency ($\sqrt{\frac{g}{\theta}\frac{d\theta}{dZ}}$), S is the vertical wind shear ($\sqrt{(\frac{dU}{dZ})^2 + (\frac{dV}{dZ})^2}$), and the overbar denotes a moving average in 200-m step to eliminate the influence of small-scale fluctuations, such as turbulence and small-scale waves. In addition, horizontal winds measured under radiosonde at the scale of a few tens of meters are affected by the chaotic movements of the gondola due to the pendulum and to the balloon's own movements (Ingleby et al., 2022). For 10-m radiosondes, the moving average in a step of 200-m could offset the effect of chaotic movements, at least to some extent. –In this case, the matching quantities that include *Ri*, wind shear, and the Brunt-Väisälä frequency between radiosonde and ERA5 profiles are actually handled in averaged 200 m intervals. The occurrence frequency of KHI is defined as the ratio of *Ri*<1/4 relative to all *Ri* calculations at a specified time period or height interval.

In Eq.(1), the length scale of overbar could potentially impact the value of *Ri*, and eventually, the occurrence frequency of KHI. In addition, the critical value of *Ri* and the vertical resolution of archived radiosonde could also cause the change in *Ri* values. The Richardson number calculated from Eq.(1) depends on the vertical resolution of the underlying data, as well as on the averaging interval. Ultimately, this influences the estimated occurrence frequency for subcritical Richardson numbers as a proxy for KHI. We resample the HVRRS dataWe resample the HVRRS data to 50 m and 100 m, and range the length scale of overbar from 100 m to 500 m, to diagnose the uncertainties raised by the length scale of segments and the vertical resolution of dataset. As indicated in Figure 1, under the same length scale of overbar, a sparser vertical grid inevitably leads to a lower occurrence frequency of subcritical *Ri*KHI. For instance, as the length scale set to 100 m, the occurrence frequency of *Ri*<1/4 at 0–2 km above sea level (a.s.la.s.l.) decreases from 22% when vertical resolution is equal to 10 m to 16% for a

设置了格式: 字体: 倾斜

设置了格式: 字体颜色: 自动设置

设置了格式: 字体: 倾斜

vertical resolution of 50 m. Moreover, a longer length-scale of segment generally yields a smaller occurrence frequency. For example, as the vertical resolution of radiosonde is equal to 10 m, the occurrence frequency at 10–15 km decreases from 9% when the length scale of segment equals 100 m to 1% when it equals 500 m. It is interesting to note that the occurrence frequency under a vertical resolution of 50 m and a segment interval of 100 m is a bit larger than that under a vertical resolution of 10 m and a segment of 200 m, possibly implying the fact that a shorter segment interval could be expected for a sparser vertical resolution. –

2.4 Gravity wave energy

The GW energy is extracted based on the broad spectral method, according to Wang and Geller (2003). In this method, the magnitude of measured zonal wind (u), meridional wind (v), and temperature (T) consisting of background states (u_0, v_0 and T_0) that are determined by applying a second-order polynomial fit (Chen et al., 2018; Zhang et al., 2022) and perturbations. Therefore, total perturbations are derived as:

$$(u', v', T') = (\mathrm{u}, \mathrm{v}, \mathrm{T}) - (u_0, v_0, T_0) \qquad (2)$$

The perturbations could include measurement noises, KH waves, GWs, and planetary waves. Only the perturbations with vertical wavelengths of 0.3–6.9 km are considered as GWs (Wang and Geller, 2003).– The mean vertical wavelength of GWs is about 2 km (Wang et al., 2005), and therefore, the lowermost threshold of 0.3 km could have little influence on the GW energy. However, the retrieval of the largest wavelength is not well determined, which is acknowledged as the radiosonde's "observational filter" (Alexander, 1998). By applying this band-pass filter, the average gravity-wave kinetic energy per unit mass (energy density) and the average potential energy density can be expressed as:

$$E_k = \frac{1}{2}\left[\overline{u'^2} + \overline{v'^2}\right] \qquad (3)$$

$$E_p = \frac{1}{2}\frac{g^2\overline{\hat{T}'^2}}{N^2} \qquad (4)$$

where g is the gravitational constant, $\hat{T}' = T'/\bar{T}$ the normalized perturbation temperature, and the overbar indicates an averaging over the tropospheric segment, which is chosen as 2–8.9 km for all regions, expect the polar region, and it is selected as 2–7.4 km for the polar region (Wang and Geller, 2003). ~~–~~Eventually, the total GW energy E_t is the sum of E_k and E_p.

3 Results and Discussions

3.1 Comparisons of wind shear between HVRRS and ERA5 reanalysis

The variations in vertical shear of horizontal wind speed and the squared Brunt-väisälä frequency entirely determine the *Ri* magnitude. Figure 2 provides an overview of the spatial distribution of wind shear at heights of 0–2 km ~~a.s.l~~a.s.l. and 10–15 km ~~a.s.l~~a.s.l. obtained from the HVRRS and ERA5 reanalysis. HVRRS-based wind shear is taken from Eq.(1), with a vertical resolution of 10-m. ~~, explicitly representing the variations of shear in the planetary boundary layer (PBL) and the upper troposphere, respectively.~~ The shear at heights of 0–2 km a.s.l.~~in the PBL regime~~ estimated by ERA5 reanalysis demonstrates a strong spatial variation, and it is largely dependent on underlying terrains and latitudes (Fig.2a). For example, large values ~~in the PBL regime~~ can most likely be observed along the coastline, which could be attributed to the prevailing sea-breeze circulation. ~~Large wind shear is common in regions where stability changes rapidly (Grasmick and Geerts, 2020).~~ As compared to the HVRRS, these shears are slightly underestimated by 5.37 ~~approximately 4~~ m/s/km, ~~–mostly~~ based on all ~~continental~~ sounding measurements (Fig.2b)~~. However, the oceanic shear is hard to be quantitatively assessed by a large number of *in-situ* radiosonde stations, with this aspect likely being evaluated by the ship-based radiosonde~~. ~~Over the tropical oceans, Savazzi et al. (2022) found the wind bias between EUREC[4]A field campaign and the ERA5 reanalysis varies greatly from day to day, attributing to the bias in wind forecasting in the ERA5 reanalysis.~~ Nevertheless, a close association between averaged ERA5-reterived shears and HVRRS-determined shears can be noticed in terms of geospatial distribution, with a correlation coefficient of 0.36 (Fig. 2b).

~~It is noteworthy that shears in the ERA5 reanalysis at heights of 10–15 km a.s.l is~~

设置了格式: 非突出显示

设置了格式: 非突出显示

设置了格式: 非突出显示

设置了格式: 字体颜色: 自动设置

~~dramatically underestimated by around 8 m/s/km, especially at middle latitudes, compared to the HVRRS.~~ It is noteworthy that shear in the ERA5 reanalysis at heights of 10–15 km a.s.l. is significantly underestimated compared to the HVRRS, especially at middle latitudes, with a mean absolute error for all stations of about 8 m/s/km (Table 1). The underestimation could partly be due to the coarse vertical resolution (around 300-m) in the ERA5 reanalysis in this height interval. However, the spatial distribution of the ERA5 shear still exhibits a significant positive correlation with the HVRRS shear, with a correlation coefficient of 0.35 (Fig.2d).

~~Following Houchi et al. (2010),~~ Following Houchi et al. (2010), the monthly shears over seven typical climate zones are separately investigated (Fig. 3), which are defined as follows: polar (70°–90°), mid latitudes (40°–70°), subtropics (20°–40°), and tropics (20°S–20°N). ~~the monthly shears over seven typical climate zones are separately investigated, which are defined as follows: Northern Hemisphere/Southern Hemisphere polar (70°–90°), Northern Hemisphere/Southern Hemisphere midlatitude (40°–70°), Northern Hemisphere/Southern Hemisphere subtropics (20°–40°), and tropics (20°S–20°N).~~ Over the polar region in the Northern/Southern Hemisphere, HVRRS-based shears are exceptionally strong in the lower stratosphere compared to those in the troposphere (Fig.3a, g), which could be attributed to the stratospheric polar jet. However, the similar altitude variation can hardly be found in ERA5-based shears that are dramatically underestimated by around 14~~6~~ m/s/km in the lower stratosphere (Fig.3h, n, also seen in Table 1). The results in midlatitudes reach a similar conclusion (Fig.3b, f, i, m). Over subtropical regions ~~in the Northern/Southern Hemisphere~~, HVRRS-based shears are consistent strong at heights of 16–21 km ~~a.s.l~~a.s.l., just above the subtropical jet stream (Fig.3c, e). However, in the ERA5 reanalysis, the region with consistently strong shears can be noticed at approximately 16 km ~~a.s.l~~a.s.l. (Fig.3j, l), which is about 3 km lower than that in the HVRRS. One possible reason might be that the model fails to resolve the further increasing shear in the lower stratosphere. ~~–~~ In the tropics, the signature of quasi-biennial oscillation (QBO) can be identified in the lower stratosphere (Fig.3d, k).

The comparison between HVRRS-based and ERA5-based shears at three typical

设置了格式: 字体颜色: 自动设置

设置了格式: 字体颜色: 自动设置

设置了格式: 非突出显示

设置了格式: 字体颜色: 自动设置

regimes is tabulated in Table 1. ~~Overall, the ERA5-based shears are underestimated at almost all investigated heights and over all climate zones, especially in the lower stratosphere. The comparison between HVRRS-based and ERA5-based shears at three typical regimes are tabulated in Table 1, representing the comparison result in the PBL region, the middle and upper troposphere, and the lower stratosphere.~~ These metrics highlight that ERA5-based shears are underestimated by approximately 5 m/s/km, 7.5 m/s/km, 10 m/s/km at heights of 0–2 km, 10–15 km, and 20–25 km ~~a.s.l~~a.s.l., respectively, which are roughly consistent with Houchi et al. (2010).

By comparison, the ERA5-acquired N^2 averaged from the surface to 30 km a.s~~g~~.l. is reliably estimated ~~over all climate zones~~at all heights, with a relative error of around 14%, as illustrated in Figure S3. This finding indicates that the ERA5 reanalysis can properly present the static stability of the background atmosphere, but it is not properly coincident with radiosonde in terms of the small-scale variability of dynamical structures. Due to a lack of global measurement of the fine-structure of the upper-air wind, however, the accuracy of ERA5-resolved shears is hard to be globally validated.

3.2 Occurrence frequency of *Ri*<1/4 in HVRRS and ERA5 reanalysis

As a prominent example, the monthly occurrence frequency of *Ri*<1/4 over the Corpus Christi station (27.77° N, −97.5° W) during years from January 2017 to October 2022 is illustrated in Figure 4. As a result, the monthly occurrence rate of *Ri*<1/4 in the planetary boundary layer (PBL) ~~PBL~~ regime determined from HVRRS is lower than the ERA5-based one, with mean values of around 10.6% and 16.9%, respectively. In the lowermost 2 km, the vertical resolution of ERA5 reanalysis is less than 200 m, and it is less than the moving segment interval in Eq.(1). The high occurrence frequency in the PBL regime could be likely related to the ~~convective activity that leads to a~~ negative or small N^2. Especially during the daytime, PBL is well mixed due to strong turbulence induced by uprising thermals (Song et al., 2018). In addition, an obvious seasonal cycle of occurrence frequencies is revealed by HVRRS in the middle and upper troposphere and has a maximum~~al~~ in ~~the~~ winter (December–

设置了格式: 字体颜色: 自动设置

设置了格式: 非突出显示

January–February) and spring ~~season~~ (March–April–May) seasons, ~~—~~ which is consistent with the finding in Zhang et al. (2019). In the vicinity of jet streams, the occurrence frequency of Ri<1/4 is generally enhanced by large wind shears. ~~H~~However, the ERA5 reanalysis does not provide such a seasonal cycle pattern, ~~owever, the ERA5 reanalysis is hard to provide such a seasonal cycle pattern,~~ and the occurrence frequency of Ri<1/4 ~~it~~ is significantly underestimated by around 8% (Fig.4b), which could be attributed to the underestimation in wind shears. In the lower stratosphere, both the HVRRS and ERA5 reanalysis provide a low estimation of occurrence frequencies, with a value of around 1%.

Furthermore, on a large spatial scale the occurrence frequency of Ri<1/4 retrieved by ERA5 reanalysis is remarkably underestimated in the free atmosphere, as compared to the HVRRS. The annual variation of the occurrence frequency of Ri<1/4 over seven climate zones at 10 to 15~~30~~ km a.s~~g~~.l. indicated by HVRRS and ERA5 reanalysis is further demonstrated in Figure 5. It is clearly seen that the occurrence frequency of Ri<1/4 provided by ERA5 reanalysis is underestimated in all months, over all climate zones, possibly implying that, in the free atmosphere, the threshold value of 1/4 in Eq.(1) is too small for the ERA5 reanalysis to capture the occurrence of KHI.

However, the ERA5 reanalysis data is non-uniformly sampled in altitude. Its vertical resolution drops from about 100-m in the boundary layer to about 500-m in the lower stratosphere. In contrast, radiosondes have a vertical resolution of 10-m at all heights. Therefore, we selected four typical heights and vertically interpolated the radiosonde to the same height resolution as ERA5 for comparison. The four height intervals are 0.8–1.3 km, 2.2–3.2 km, 6–15 km and 20–21 km a.s.l., as shown in Table 2. In these height intervals, the vertical resolution of ERA5 is about 100-m, 200-m, 300-m and 400-m respectively. Even at the same vertical resolution, ERA5 still seriously underestimates the value of OF(Ri<1/4) at all heights and all climate zones. These results indicate that the greatest difficulty in evaluating subcritical Ri with ERA5 is that its simulation of wind shears might be seriously underestimated compared with radiosonde. As illustrated in Table 3, even accounting for the fact that ERA5 has a comparable vertical resolution of radiosonde, wind shears in ERA5 reanalysis are still

设置了格式: 字体颜色: 自动设置

设置了格式: 非突出显示

设置了格式: 非突出显示

带格式的: 缩进: 首行缩进: 2 字符

设置了格式: 字体: 倾斜

设置了格式: 字体: 倾斜

设置了格式: 字体: 倾斜

underestimated by around 51.9%, 50.7%, 44.5%, and 62.5% at 0.8–1.3 km, 2.2–3.2 km, 6–15 km and 20–21 km a.s.l., respectively. In order to obtain an occurrence frequency of subcritical *Ri* from ERA5 reanalysis that is comparable with radiosonde-based *OF*(*Ri*<1/4), the *Rit* for ERA5 should be set larger than 1/4. For instance, at

0.8–1.3 km and 2.2–3.2 km a.s.l., the *Rit* equals 1 could be a proper choice for ERA5 reanalysis, rather than 1/4 (Table 2). More generally, 0.5<*Rit*<1.5 could be more suitable for ERA5 reanalysis, compared to *Rit*=1/4.

Due to the huge change in the vertical resolution of ERA5, it could be difficult to interpolate ERA5 into uniform data vertically with a relatively high resolution. Therefore, the question posed here is, what is the proper threshold value of *Ri* in predicting the occurrence of KHI when using the ERA5 reanalysis, compared to HVRRS? The occurrence frequency of *Ri*<1/4 indicated by the HVRRS, the ERA5-determined occurrence frequencies produced by *Ri*<0.25, *Ri*<0.5, *Ri*<1, *Ri*<1.5, and *Ri*<2 at all heights up to 30 km ~~a.s.l~~a.s.l. are demonstrated in Figure 6. It is notable that over all climate zones and in the free atmosphere, occurrence frequencies of *Ri*<0.25 and *Ri*<0.5 obtained from the ERA5 reanalysis are underestimated~~undervalued~~, but the frequencies of *Ri*<1.5 and *Ri*<2 are generally overestimated~~valued~~. T~~Among others, t~~he occurrence frequency of *Ri*<1 gives a close estimation both in magnitude and spatial variation compared to HVRRS over all climate zones.

Furthermore, the correlation coefficients between HVRRS-determined ~~KHI~~ occurrence frequency and the ERA5-determined frequencies indicated by different threshold values of *Ri* at height levels of 0 to 30 km are illustrated in Figure 7. It is worth noting that, in the troposphere, the ERA5-based frequencies indicated by *Ri*<1, *Ri*<1.5, and *Ri*<2 are highly positively correlated with those from the HVRRS, with a correlation coefficient of around 0.6 over all climate zones. In the lower stratosphere, however, these coefficients rapidly decline to 0.1, which can be explained by the low occurrence frequency ~~of KHI~~ in this height regime.

Combined the findings in Figures 6 and 7, in the free troposphere, we can conclude that the ERA5-determined occurrence frequency of *Ri*<1 is closest to the frequency of *Ri*<1/4 based on the HVRRS. In the free atmosphere, KHI is the dominant source for

设置了格式: 字体: 倾斜
设置了格式: 字体: 非倾斜
设置了格式: 字体: 倾斜
设置了格式: 字体: 非倾斜
设置了格式: 字体: 非倾斜
设置了格式: 字体: 非倾斜
设置了格式: 字体: 非倾斜
设置了格式: 字体: 非倾斜
设置了格式: 字体: 非倾斜
设置了格式: 字体: 非倾斜
设置了格式: 字体: 非倾斜
设置了格式: 字体: 非倾斜
设置了格式: 字体颜色: 自动设置

clear-air turbulence (CAT) that is a well-known hazard to aviation. Therefore, the global characterization of KHI occurrence frequency in the free atmosphere obtained from ERA5 reanalysis could be of importance for understanding the spatial-temporal variation of CAT. In the following sections, the occurrence frequency of ~~KHI~~ subcritical *Ri* (hereinafter ~~*OF*(KHI)~~*OF*(*Ri*<*Rit*)) is based on *Ri*<1 in ERA5 reanalysis and *Ri*<1/4 in HVRRS, unless otherwise noted.

Finally, it is noteworthy that *OF*(*Ri*<*Rit*) includes the component of *Ri*<0 that indicates potential for convective instability. However, both ERA5 and HVRRS are difficult to totally avoid *Ri*<0 when calculating *Ri*. Therefore, we evaluated the proportion of *Ri*<0 in all *Ri*<*Rit* in the two datasets to evaluate the possible contribution from convection, as shown in Figure 8. For HVRRS, the proportion of *OF*(*Ri*<0) drops sharply from about 40% in the PBL region to about 18% at 5–15 km a.s.l.. Similarly, for ERA5 its proportion drops from about 40% in the lowermost part of the atmosphere to about 2% at 5–16 km a.s.l.. These findings indicate that, in the free atmosphere, *OF*(*Ri*<*Rit*) is mainly composed of *OF*(0<*Ri*<*Rit*), which implies that local instabilities constitute most of the dynamic instability.

~~3.4~~ 3.3 The ~~*OF*(KHI)~~ *OF*(*Ri*<*Rit*) climatology

For a first hint the global distributions of ~~*OF*(KHI)~~ *OF*(*Ri*<*Rit*) provided by the ERA5 reanalysis at 0–2 km ~~a.s.l~~a.s.l. and 10–15 km ~~a.s.l~~a.s.l. are displayed in Figure 9~~8~~. *OF*(*Ri*<*Rit*) ~~*OF*(KHI)~~ in the PBL region is considerably spatially heterogeneous. Over subtropical oceans in the Northern/Southern Hemisphere, the intense *OF*(*Ri*<*Rit*) ~~*OF*(KHI)~~ can be noticed and has a magnitude of around 50% (Fig.9~~8~~a). In addition, over the Sahara Desert the ~~*OF*(KHI)~~*OF*(*Ri*<*Rit*) reaches as high as 65%. Interestingly, the spatial variation in *OF*(*Ri*<*Rit*) –ensembled by years 2017 to 2022 ~~in *OF*(KHI)~~ keeps high consistency with that of planetary boundary layer height (PBLH) over oceans, such as the Pacific Ocean near Japan and the Atlantic Ocean near U.S., as shown in Figure S4. However, at 0–2 km a.s.l., the spatial variation of *OF*(0<*Ri*<*Rit*) exhibits

设置了格式: 字体: 倾斜
设置了格式: 字体: 非倾斜
设置了格式: 字体: 非倾斜
设置了格式: 字体: 倾斜
设置了格式: 字体: 倾斜
设置了格式: 字体: 倾斜
带格式的: 无项目符号或编号
设置了格式: 字体: 倾斜
设置了格式: 字体: 倾斜
设置了格式: 字体: 倾斜

a large difference with that of $OF(Ri<Rit)$ in terms of magnitude, as shown in Figure S5. It is around 40% (20%) lower than that of $OF(Ri<Rit)$ over subtropical oceans (Australia and North Africa). ~~Usually, in the PBL regime, a deeper PBLH that represents more vigorous convection activities can predict a higher *OF*(KHI). These findings suggest that, in the PBL regime, the burst of KHI is likely closely associated with thermal convection due to the heating of the ground.~~ A~~Similarly, a~~t heights of 10–15 km ~~a.s.l~~a.s.l., intensive ~~*OF*(KHI)~~ $OF(0<Ri<Rit)$ can be viewed over subtropic regions and has a value of around 10% (Fig.9~~8~~b), which is likely attributed to upper tropospheric jets.

In comparison, the spatial-temporal variability of ~~*OF*(KHI)~~$OF(Ri<Rit)$ indicated by HVRRS keeps highly ~~high~~ consistency with that of ERA5 reanalysis over all climate zones and in the free troposphere~~at all heights up to 30 km~~, except in the stratosphere of polar region (Figure 10~~9~~)~~, especially in the free troposphere~~. ~~Obvious~~ S~~s~~easonal cycles can be detected by both the HVRRS and ERA5 reanalysis over all climate zones, especially over subtropics and midlatitude regions~~subtropics and midlatitude regions in the troposphere by both the HVRRS and ERA5 reanalysis~~. However, the ERA5-based ~~*OF*(KHI)~~ $OF(Ri<Rit)$ can only reflect the large scale structure ~~backbone~~ of the cycles, and it is hard to quantify the detailed variation like the HVRRS does. ~~For regions without high resolved wind and temperature measurements, the ERA5 model product could be a good choice to represent the thermodynamic instability of background atmosphere. Although ERA5-based *OF*(KHI) is consistent with the HVRRS-based one from a global perspective, it is generally underestimated over polar regions (Fig.9a, g, h, n).~~

Furthermore, the seasonal variation of $OF(Ri<Rit)$ with Rit=1/4 for HVRRS and Rit=1 for ERA5 for all climate zones is further analyzed in Figure 11. In the midlatitudes and subtropics, the $OF(Ri<Rit)$ exhibits maximum values in the PBL, as well as a local minimum in the middle troposphere and a local maximum at altitudes around 9 km. In the stratosphere the occurrence frequencies decrease to values of the order of 1% (Fig.11b,c,e,f)~~the seasonal variation of *OF*(KHI) over seven climate zones indicated by two datasets is shown in Figure 10. Over midlatitude and subtropics~~

设置了格式: 字体颜色: 自动设置
设置了格式: 字体颜色: 自动设置
设置了格式: 字体: 倾斜, 字体颜色: 自动设置
设置了格式: 字体颜色: 自动设置
设置了格式: 字体: 倾斜, 字体颜色: 自动设置
设置了格式: 字体颜色: 自动设置
设置了格式: 字体颜色: 自动设置
设置了格式: 字体颜色: 自动设置
设置了格式: 字体颜色: 自动设置
设置了格式: 字体颜色: 自动设置

~~regions, the *OF*(KHI) quickly decreases from around 40% in the PBL regime to around 6% at around 3 km and then increases to around 8% at around 9 km, and eventually, it decreases to around 2% in the lower stratosphere (Fig.10b,c,e,f).~~. Over tropic regions, a primary peak can be clearly noticed at around 13 km, with a maximum of 12% for the HVRRS and 20% for the ERA5 reanalysis (Fig.11~~0~~d, k). The seasonality over the tropical region could be related to some large scale flow features like the Summer Asian Monsoon and the tropical easterly jet (Roja Raman et al., 2009; Sunilkumar et al., 2015; Kaluza et al., 2021). Over polar regions, the tropospheric ~~*OF*(KHI)~~*OF*(*Ri*<*Rit*) is significantly lower than that over other climate zones, with values ranging from around 4% at heights of 2–8 km to 1% in the lower stratosphere (Fig.11~~0~~a,g).

设置了格式: 字体颜色: 自动设置

~~As well, the latitude-altitude variation of ERA5 reterived *OF*(KHI) is clearly notable. In the free atmosphere the highest occurrences can be noticed at height intervals of 8–15 km over tropical zones in all seasons, with magnitudes of around 30%. A poleward decrease pattern can be clearly detected in all seasons, with values varying from 30% at low latitudes to around 5% at high latitude in the middle and upper troposphere, which is consistent with the report in Zhang et al. (2022).~~

带格式的: 缩进: 首行缩进: 0.74 厘米

In Table 4~~2~~, the mean ~~*OF*(KHI)~~*OF*(*Ri*<*Rit*) magnitudes over seven climate zones and at three typical altitude regimes are listed. ~~In the PBL~~At 0–2 km a.s.l., the ERA5-based ~~*OF*(KHI)~~*OF*(*Ri*<*Rit*) is about 20% larger than that of the HVRRS-based one. At 10–15 km a.s.l.~~In the middle and upper stratosphere~~, the ERA5-based ~~*OF*(KHI)~~*OF*(*Ri*<*Rit*) is reasonably well estimated, except that it is overestimated by around 5.8% over the tropics region. In addition, ERA5 underestimates ~~*OF*(KHI)~~*OF*(*Ri*<*Rit*) by around 0.5% in the lower stratosphere.

According to Fig.9~~8~~a, it seems that low-level continental ~~*OF*(KHI)~~*OF*(*Ri*<*Rit*) –is dependent on underlying terrains. However, the vertical resolution of ERA5 in the PBL decreases sharply, leading to the fact that the resolution of the PBL data over the region with high elevations can be significantly lower than that of regions with low elevations, which could bring great challenges to the analysis of the impact of topography on low-level *OF*(*Ri*<*Rit*). –Therefore, we investigate the association of low-level HVRRS-determined ~~*OF*(KHI)~~*OF*(*Ri*<*Rit*) –with the standard deviation of orography (SDOR).

At heights of 1–2 km a.g.l., the underlying terrain with a large SDOR generally corresponds to a high ~~*OF*(KHI)~~*OF*(*Ri*<*Ri*t), with a correlation coefficient between ~~*OF*(KHI)~~*OF*(*Ri*<*Ri*t) and SDOR of 0.24. Then, the coefficient decreases to 0.15 at 3–4 km a.g.l. (Fig.12~~1~~b), and eventually, it equals 0.14 at 5–6 km a.g.l. (Fig.12~~1~~c). These findings indicate that, complex terrain may locally enhance ~~over mountainous areas, a high low-level~~ ~~*OF*(KHI)~~*OF*(*Ri*<*Ri*t) ~~would be expected~~.

Moreover, it is quite evident from Fig.9~~8~~b and Fig.S5 that both ~~the~~ ~~*OF*(KHI)~~*OF*(*Ri*<*Ri*t) and *OF*(0<*Ri*<*Ri*t) are~~is~~ largely enhanced over the tropical ocean associated with the El Niño Southern Oscillation (~~ENSO~~ENSO) ~~events~~. The most of the enhanced ~~*OF*(KHI)~~*OF*(*Ri*<*Ri*t) can be identified over the Niño 3 region (5° N–5° S, 150° W–90° W), and the time-height cross section of ~~*OF*(KHI)~~ *OF*(*Ri*<*Ri*t) during years of 2000 to 2022 is illustrated in Figure 13~~2~~. The ~~*OF*(KHI)~~*OF*(*Ri*<*Ri*t) at height region of 6–13 km are evidently large, with values of around 40%, which is about 20% larger than the climatological mean value (Fig.10~~9~~j). More specifically, ~~*OF*(KHI)~~*OF*(*Ri*<*Ri*t) during time periods of La Niña~~o~~ events is obviously stronger than that during the EI Niño periods. The identification of ENSO events is based on Ren et al. (2018), Li et al. (2022), and Lv et al. (2022). It is also worth recalling here that the wind shear does not exhibit such an anomaly over the Niño 3 region (Fig.2c), implying that the ~~*OF*(*KHI*)~~ *OF*(*Ri*<*Ri*t) anomaly could likely be attributed to the ENSO-related tropical convective heating in the upper troposphere, leading to a low Brunt-Väisälä frequency.

3.4 The dynamical environment of *OF*(*Ri*<*Ri*t) in the free troposphere~~KHI~~

~~In the PBL, the raised KHI could be attributed to the interaction between complex terrain and low-level wind and thermal convection. While i~~In the free troposphere ~~atmosphere~~ where the convection activity is generally weak, KHI is preferentially generated from strong wind shear, which may be~~is~~ closely associated with mean flows and wave activities.

~~We first evaluate the association of low level *OF*(KHI) with near surface wind~~

设置了格式: 字体: 倾斜
设置了格式: 字体: 倾斜
设置了格式: 字体: 倾斜

speed for the HVRRS station with a SDOR greater than 50 (Figure 13). It is probably not surprising that the *OF*(KHI) is positively correlated with near surface wind speed at both heights of 1–2 km and 3–4 km a.g.l, with correlation coefficients of 0.09 and 0.04, respectively. These low coefficients could be attributed to too large samples. Therefore, we infer that the interaction between near-surface winds and complex terrains could increase the magnitude of low-level *OF*(KHI).

——The propagation of GW could raise strong wind shear, and therefore generate KHI. Thereby, we investigate the joint distribution of *OF*(KHI)$OF(Ri<Rit)$ with tropospheric GW total energy and wind shear (Figure 14). The latitudinal variation of GW total energy exhibits a double-peak structure, with two peaks at around 30° in the Northern/Southern Hemisphere (Fig.14a). The joint distribution of $OF(Ri<Rit)$ with GW energy and wind shear indicates that large $OF(Ri<Rit)$ (for instance, larger than 10%) generally corresponds to GW energy larger than 10 J/kg or wind shear exceeds 14 m/s/km (Fig. 14b). Also, $OF(0<Ri<Rit)$ exhibits a similar distribution (Figure S6). Overall, $OF(Ri<Rit)$ obviously increases with GW total energy (Figure S9a), possibly implying that the propagation of GWs could enhance wind shear and therefore, the burst of KHI.Overall, large *OF*(KHI) always corresponds to strong GW activities and large wind shears, likely indicating that GW activity is crucial for the occurrence of KHI.

In addition, the interaction between low-level wind and mountain barrier could be a source of orographic GWs (Zhang et al., 2022). We take orographic GW dissipation in ERA5 reanalysis, which is the accumulated conversion of kinetic energy in the mean flow into heat over the whole atmospheric column, as an indicator of the strength of orographic GWs. It is interesting to note that monthly averaged orographic GW dissipation and monthly ERA5-determined *OF*(KHI) $OF(Ri<Rit)$ at heights from ground up to 30 km demonstrates a close association (Figure S75). For instance, in the middle troposphere, they are positively associated over mountainous areas such as the Rocky Mountains and the Alps Mountain, with correlation coefficients of around 0.5. These findings also suggest that the propagation of orographic GWs could be a potential source for KHI. during months with strong unresolved gravity wave activity, which then modify the flow and stability parameters of the resolved flow, and result in an

enhanced $OF(Ri<Rit)$.

At jet heights (10–15 km a.g.l.), a large shear can beis easily induced by strong wind speed. Figure 15 demonstrates the joint distribution of OF(KHI)$OF(Ri<Rit)$ with wind speed and wind shear. Similarly, large OF(KHI)$OF(Ri<Rit)$ (> 10%) can be easily found when the wind speed exceeds 250 m/s and wind shear is larger than 20 m/s/km. In addition, $OF(0<Ri<Rit)$ can draw a similar conclusion (Figure S8). In the middle and upper troposphere, $OF(Ri<Rit)$ almost linearly increases with wind speed (Figure S9b).However, it is clear that large wind speed is not a necessary condition for KHI. The occurrence of KHI favors the mean flow with a speed exceeding 20 m/s, but it does not ensure to happen for an extremely large wind speed.

In a short conclusion, in the free troposphere, the occurrence of KHI would favors the dynamical environment with strong orographic or non-orographic GW activities and relatively large mean flow (around >250 m/s).

4 Conclusion and remarks

The occurrence of KHI is potential crucial for many implications, such as aircraft safety and , mass transfer, and climate change, just name a few, but it is very hard to be globally understood due to its fine structure. The subcritical Richardson number is commonly used as an indictor for KHI.This analysis uses high-resolution model products and radiosondes to globally characterize the distribution of KHI occurrence frequency from the years 2017 to 2022. This study uses the ERA5 as the latest reanalysis product from the ECMWF as well as a comprehensive data set of HVRRS radiosonde soundings to globally characterize the distribution of low Richardson numbers as a proxy for the occurrence of KHI, for the years 2017 to 2022.

Vertical wWind shears are considerably underestimated at almost all heights and over all climate zones by the ERA5 reanalysis, compared to the HVRRS. It is noteworthy that vertical wind shear shears in the ERA5 reanalysis at heights of 10–15 km a.s.la.s.l. is dramatically underestimated by around 8 m/s/km, especially at middle

设置了格式: 字体颜色: 自动设置

设置了格式: 图案: 清除

设置了格式: 图案: 清除

设置了格式: 非突出显示

设置了格式: 字体颜色: 自动设置

设置了格式

设置了格式: 字体颜色: 自动设置

latitudes. However, the spatial distribution of the ERA5 shear exhibits a statistically significant positive correlation with the HVRRS shear. ~~The underestimation therefore influences the performance of KHI analysis.~~ As a result, the ERA5-determined occurrence frequency of $Ri<1/4$ ~~in the free tropospheric~~ is significantly underestimated. In addition, it is ~~poorly~~ weak correlated with HVRRS-determined ones at ~~all~~ most heights and over ~~all~~ most climate zones.

However, the vertical resolution of ERA5 reanalysis sharply decreases with altitude, which is not comparable with HVRRS. Thus, to match with ERA5 reanalysis at specified height intervals, the HVRRS was vertically interpolated with resolutions spanning from 100-m to 400-m. Even at a comparable resolution, vertical wind shear is underestimated by around 50%, leading to a considerable underestimation in $OF(Ri<1/4)$, compared to radiosondes.

Interestingly, the ERA5-determined occurrence frequency of $Ri<1$ is ~~highly~~ generally consistent with the frequency of $Ri<1/4$ obtained from HVRRS, in terms of magnitude and temporal variation. Rather than $Ri<1/4$, we argue that the threshold value of $Ri<1$ could be more proper when using ERA5 reanalysis for KHI study, especially in the middle and upper troposphere over midlatitude and subtropic regions in the Northern/Southern Hemisphere, where a high consistency between HVRRS and ERA5 has been found in terms of $OF(Ri<Rit)$ magnitude. –In other words, under a similar occurrence frequency, the identification of vertical segments with $Ri<1$ in ERA5 is equitable with identification of vertical segments with $Ri<1/4$ using HVRRS.

~~The climatology of *OF*(KHI) exhibits significant seasonal cycles over polar, midlatitude, and subtropic regions.~~ The climatology of $OF(Ri<Rit)$ exhibits significant seasonal cycles over all latitudes. A poleward decrease can be clearly identified in the middle and upper troposphere. In addition, over mountainous area, ~~the low-level *OF*(KHI)~~ complex terrain may locally enhance low-level $OF(Ri<Rit)$. ~~is positively sensitive to the standard deviations of orography.~~ Moreover, it is immediately obvious that the both $OF(Ri<Rit)$ and $OF(0<Ri<Rit)$ ~~*OF*(KHI)~~ in the middle and upper

设置了格式: 字体: 倾斜
设置了格式: 字体: 倾斜
设置了格式: 字体: 倾斜
设置了格式: 字体: 倾斜
设置了格式: 字体: 倾斜
带格式的: 缩进: 首行缩进: 0.74 厘米
设置了格式: 字体颜色: 自动设置
设置了格式: 字体: 倾斜
设置了格式: 字体颜色: 自动设置
设置了格式: 非突出显示
设置了格式: 非突出显示

troposphere of the Niño 3 region is largely enhanced probably by the tropical convective heating.

Moreover, both $OF(Ri<Rit)$ and $OF(0<Ri<Rit)$ exhibit close relationship with GW activities and background mean flow. For instance, large $OF(Ri<Rit)$ (>10%) favors GW energy larger than 10 J/kg or mean flow stronger than 25 m/s. Over complex terrains, the orographic GW breaking could locally enhance $OF(Ri<Rit)$. ~~Over the mountainous area, the low-level *OF*(KHI) favors large near-surface wind speed. In the free troposphere, the *OF*(KHI) favors intensive orographic or non-orographic GW activities and relatively large mean flow (>20 m/s).~~

~~Those findings could be valuable for pointing out the performance of ERA5 reanalysis in terms of representing KHI occurrence frequency, as compared to a near-global high-resolution radiosonde measurement.~~ Those findings are valuable for pointing out the performance of the ERA5 reanalysis in terms of resolving low Richardson numbers as a proxy for KHI, in comparison with a near-global high-resolution radiosonde measurement. In addition, the spatial-temporal variability of ~~*OF*(KHI)~~$OF(Ri<Rit)$ over different climate zones from near-ground up to 30 km is quantitatively characterized by ERA5 and HVRRS, which could provide new insights that increase our understanding of the fine structure of upper air.

设置了格式: 非突出显示
带格式的: 缩进: 首行缩进: 0 厘米
设置了格式: 非突出显示
设置了格式: 非突出显示
设置了格式: 非突出显示
设置了格式: 字体颜色: 自动设置
设置了格式: 字体颜色: 自动设置
带格式的: 缩进: 首行缩进: 0 厘米

Acknowledgement

The authors would like to acknowledge the National Meteorological Information Centre (NMIC) of CMA, NOAA, Deutscher Wetterdienst (Climate Data Center), U.K Centre for Environmental Data Analysis (CEDA), GRUAN, ECMWF, and the University of Wyoming for continuously collecting and generously providing high-resolution radiosonde data. Last but not least, we would like to thank two anonymous reviewers for their excellent comments that greatly helped to improve our work.

Financial support

This study jointly supported by the National Natural Science Foundation of China under grants 42205074, 42127805, and 62101203, the Hubei Provincial Natural Science Foundation of China under Grant 2021CFB459, and the Research Grants of Huazhong Agricultural University under grants No. 2662021XXQD002 and 2662021JC008.

Competing interests

The contact author has declared that neither they nor their co-authors have any competing interests

Data availability

The dataset can be accessed at ECMWF (2022).

Author contributions

JZ conceptualized this study. JS carried out the analysis with comments from other co-authors. JZ wrote the original manuscript. WW, SZ, TY, WD provided useful suggestions for the study. All authors contributed to the improvement of paper.

References

Alexander, M. J.: Interpretations of observed climatological patterns in stratospheric gravity wave variance, J. Geophys. Res. Atmos., 103(D8), 8627–8640, https://doi.org/10.1029/97JD03325, 1998.

Baumgarten, G., and Fritts, D. C.: Quantifying Kelvin-Helmholtz instability dynamics observed in noctilucent clouds: 1. Methods and observations, J. Geophys. Res. Atmos., 119, 9324–9337, https://doi.org/10.1002/2014JD021832, 2014.

Duruisseau, F., N., Huret, A., Andral, and Camy-Peyret, C.: Assessment of the ERA-Interim winds using high-altitude stratospheric balloons, J. Atmos. Sci., 74(6), 2065–2080, https://doi.org/10.1175/JAS-D-16-0137.1, 2017.

Dong, W., Fritts, D. C., Lund, T. S., Scott, A.W., and Zhang, S: Self-acceleration and Instability of Gravity Wave Packets: 2. Two-Dimensional Packet Propagation, Instability Dynamics, and Transient Flow Responses, J. Geophys. Res. Atmos., https://doi.org/10.1029/2019JD030691, 2020.

Dong, W., Fritts, D. C., Thomas, G. E., and Lund, T. S.: Modeling responses of polar mesospheric clouds to gravity wave and instability dynamics and induced large-scale motions, J. Geophys. Res. Atmos., 126, e2021JD034643. https://doi.org/10.1029/2021JD034643, 2021.

Dong, W., Fritts, D. C., Hickey, M. P., Liu, A. Z., Lund, T. S., Zhang, S., et al.: Modeling studies of gravity wave dynamics in highly structured environments: Reflection, trapping, instability, momentum transport, secondary gravity waves, and induced flow responses, J. Geophys. Res. Atmos., 127, e2021JD035894. https://doi.org/10.1029/2021JD035894, 2022.

ECMWF: ECMWF Reanalysis v5 (ERA5), European Centre for Medium-Range Weather Forecasts [data set], https://www.ecmwf.int/en/forecasts/dataset/ecmwf-reanalysis-v5, last access: 07 December 2022.

Fritts, D. C., K. Wan, J. Werne, T. Lund, and Hecht, J. H.: Modeling the implications of

设置了格式: 字体颜色: 自动设置

Kelvin-Helmholtz instability dynamics for airglow observations, J. Geophys. Res. Atmos., 119, 8858–8871, https://doi.org/10.1002/2014JD021737, 2014.

Fritts, D. C., P. M. Franke, K. Wan, T. Lund, and Werne, J.: Computation of clear-air radar backscatter from numerical simulations of turbulence: 2. Backscatter moments throughout the lifecycle of a Kelvin Helmholtz instability, J. Geophys. Res., 116, D11105, https://doi.org/10.1029/2010JD014618, 2011.

Fritts, D. C., and Rastogi, P. K.: Convective and dynamical instabilities due to gravity wave motions in the lower and middle atmosphere: Theory and observations. Radio Sci., 20, 1247–1277, https://doi.org/10.1029/RS020i006p01247, 1985.

Fritts, D. C., L., Wang, T. S., Lund, S. A., Thorpe, C. B., Kjellstrand, B., Kaifler, and Kaifler, N.: Multi-Scale Kelvin-Helmholtz instability dynamics observed by PMC Turbo on 12 July 2018: 2. DNS modeling of KHI dynamics and PMC responses., J. Geophys. Res. Atmos., 127, e2021JD035834. https://doi.org/10.1029/2021JD035834, 2022.

~~Fritts, D. C., Dong, W., Lund, T. S., and Brain., L.: Self Acceleration and Instability of Gravity Wave Packets: 3. Three Dimensional Packet Propagation, Secondary Gravity Waves, Momentum Transport, and Transient Mean Forcing in Tidal Winds, J. Geophys. Res. Atmos., https://doi.org/10.1029/2019JD030692, 2020.~~

Grasmick, C., and Geerts, B.: Detailed dual-Doppler structure of Kelvin–Helmholtz waves from an airborne profiling radar over complex terrain. Part I: Dynamic structure, J. Atmos. Sci., 77(5), 1761–1782., https://doi.org/10.1175/JAS-D-19-0108.1, 2020.

Gavrilov, N. M., Luce, H., Crochet, M., Dalaudier, F., and Fukao, S.: Turbulence parameter estimations from high-resolution balloon temperature measurements of the MUTSI-2000 campaign, Ann. Geophys., 23, 2401–2413, doi:10.5194/angeo-23-2401-2005, 2005

Guo, J., Zhang, J., Yang, K., Liao, H., Zhang, S., Huang, K., Lv, Y., Shao, J., Yu, T., Tong, B., Li, J., Su, T., Yim, S. H. L., Stoffelen, A., Zhai, P., and Xu, X.: Investigation of near-global daytime boundary layer height using high-resolution radiosondes: first results and comparison with ERA5, MERRA-2, JRA-55, and NCEP-2 reanalyses, Atmos. Chem. Phys., 21, 17079–17097, https://doi.org/10.5194/acp-21-17079-2021, 2021.

Haack, A., M. Gerding, and Lübken, F.-J.: Characteristics of stratospheric turbulent layers measured by LITOS and their relation to the Richardson number, J. Geophys. Res. Atmos., 119, 10605–10618, https://doi.org/10.1002/2013JD021008, 2014.

Hersbach, H., Bell, B., Berrisford, P., Hirahara, S., Horányi, A., Muñoz-Sabater, J., Nicolas, J., Peubey, C., Radu, R., Schepers, D., Simmons, A., Soci, C., Abdalla, S., Abellan, X., Balsamo, G., Bechtold, P., Biavati, G., Bidlot, J., Bonavita, M., De Chiara, G., Dahlgren, P., Dee, D., Diamantakis, M., Dragani, R., Flemming, J., Forbes, R., Fuentes, M., Geer, A., Haimberger, L., Healy, S., Hogan, R. J., Hólm, E., Janisková, M., Keeley, S., Laloyaux, P., Lopez, P., Lupu, C., Radnoti, G., de Rosnay, P., Rozum, I., Vamborg, F., Villaume, S., and Thépaut, J.-N.: The ERA5 global reanalysis, Q. J. Roy. Meteorol. Soc., 146, 1999–2049, https://doi.org/10.1002/qj.3803, 2020.

Homeyer, C. R., L. L. Pan, and Barth, M. C.: Transport from convective overshooting of the extratropical tropopause and the role of large-scale lower stratospheric stability, J. Geophys. Res. Atmos., 119(5), 2220–2240, https://doi.org/10.1002/2013JD020931, 2014.

Houchi, K., Stoffelen, A., Marseille, G. J., and De Kloe, J.: Comparison of wind and wind shear climatologies derived from high-resolution radiosondes and the ECMWF model, J. Geophys. Res.-Atmos., 115, D22123, https://doi.org/10.1029/2009JD013196, 2010.

Ingleby, B., Motl, M., Marlton, G., Edwards, D., Sommer, M., von Rohden, C., Vömel, H., and Jauhiainen, H.: On the quality of RS41 radiosonde descent data, Atmos. Meas. Tech., 15, 165–183, https://doi.org/10.5194/amt-15-165-2022, 2022.

Lee, S. H., Williams, P. D., and Frame, T. H.: Increased shear in the North Atlantic upper-level jet stream over the past four decades, Nature, 572, 639–642, https://doi.org/10.1038/s41586-019-1465-z, 2019.

Lee, J. H., Kim, J.-H., Sharman, R. D., Kim, J., & Son, S.-W. Climatology of Clear-Air

设置了格式: 字体: (默认) Times New Roman, 小四

Turbulence in upper troposphere and lower stratosphere in the Northern Hemisphere using ERA5 reanalysis data. Journal of Geophysical Research: Atmospheres, 128, e2022JD037679. https://doi.org/10.1029/2022JD037679, 2023.

Li, X., Hu, Z. Z., Tseng, Y. H., Liu, Y., and Liang, P.: A historical perspective of the La Niña event in 2020/2021, J. Geophys. Res.-Atmos., 127(7), e2021JD035546, https://doi.org/10.1029/2021JD035546, 2022.

Lv, A., Fan, L., and Zhang, W.: Impact of ENSO Events on Droughts in China, Atmosphere, 13(11), 1764, https://doi.org/10.3390/atmos13111764, 2022.

Jaeger, E. B., and Sprenger, M.: A Northern Hemispheric climatology of indices for clear air turbulence in the tropopause region derived from ERA40 reanalysis data, J. Geophys. Res., 112, D20106, doi:10.1029/2006JD008189, 2007.

Kaluza, T., Kunkel, D., and Hoor, P.: On the occurrence of strong vertical wind shear in the tropopause region: a 10-year ERA5 northern hemispheric study, Weather Clim. Dynam., 2, 631–651, https://doi.org/10.5194/wcd-2-631-2021, 2021.

Kunkel, D., Hoor, P., Kaluza, T., Ungermann, J., Kluschat, B., Giez, A., Lachnitt, H.-C., Kaufmann, M., and Riese, M.: Evidence of small-scale quasi-isentropic mixing in ridges of extratropical baroclinic waves, Atmos. Chem. Phys., 19, 12607–12630, https://doi.org/10.5194/acp-19-12607-2019, 2019.

Ko, H. C., H. Y., Chun, R., Wilson, and Geller, M. A.: Characteristics of atmospheric turbulence retrieved from high vertical-resolution radiosonde data in the United States, J. Geophys. Res. Atmos., 124.https://doi.org/10.1029/2019JD030287, 2019.

Ko, H. C. and Chun, H. Y.: Potential sources of atmospheric turbulence estimated using the Thorpe method and operational radiosonde data in the United States. Atmos. Res., 265, 105891, https://doi.org/10.1016/j.atmosres.2021.105891, 2022.

Muschinski, A., and Wode, C.: First in situ evidence for coexisting submeter temperature and humidity sheets in the lower free troposphere, J. Atmos. Sci., 55(18), 2893–2906, https://doi.org/10.1175/1520-0469(1998)055<2893:FISEFC>2.0.CO;2, 1998.

设置了格式: 字体: (默认) Times New Roman, 小四

设置了格式: 字体颜色: 自动设置

设置了格式: 字体颜色: 自动设置

设置了格式: 字体颜色: 自动设置

设置了格式: 字体颜色: 自动设置

设置了格式: 字体颜色: 自动设置

设置了格式: 字体颜色: 自动设置

North, G. R., Pyle, J. A., and Zhang, F.: Encyclopedia of atmospheric sciences, Academic Press, Cambridge, Massachusetts, United States, 224 pp., 2014

Plougonven, R., and Zhang, F.: Internal gravity waves from atmospheric jets and fronts, Rev. Geophys., *52*, 33–76, https://doi.org/10.1002/2012RG000419, 2014.

~~Rennie, M. P., Isaksen, L., Weiler, F., de Kloe, J., Kanitz, T., and Reitebuch, O.: The impact of Aeolus wind retrievals on ECMWF global weather forecasts, Q. J. Roy. Meteorol. Soc., 147(740), 3555–3586, https://doi.org/10.1002/qj.4142, 2021.~~

Ren, H. L., B., Lu, J., Wan, B., Tian, and Zhang, P.: Identification standard for ENSO events and its application to climate monitoring and prediction in China, J. Meteorol. Res., 32, 923–936, https://doi.org/10.1007/s13351-018-8078-6, 2018.

Roja Raman, M., Jagannadha Rao, V. V., Venkat Ratnam, M., Rajeevan, M., Rao, S. V., Narayana Rao, D., and Prabhakara Rao, N.: Characteristics of the Tropical Easterly Jet: Long-term trends and their features during active and break monsoon phases, J. Geophys. Res.-Atmos., 114, 1–14, https://doi.org/10.1029/2009JD012065, 2009.

Sandu, I., A., A., van Niekerk, T. G., Shepherd, S. B., Vosper, A., Zadra, J., Bacmeister, et al: Impacts of orography on large-scale atmospheric circulation. npj Clim Atmos Sci, 2(1), 1–8, https://doi.org/10.1038/s41612-019-0065-9, 2019.

Savazzi, A. C. M., Nuijens, L., Sandu, I., George, G., and Bechtold, P.: The representation of the trade winds in ECMWF forecasts and reanalyses during EUREC^{4}A, Atmos. Chem. Phys., 22, 13049–13066, https://doi.org/10.5194/acp-22-13049-2022, 2022.

Sharman, R. D., S. B. Trier, T. P. Lane, and Doyle., J. D.: Sources and dynamics of turbulence in the upper troposphere and lower stratosphere: A review, Geophys. Res. Lett., 39, L12803, https://doi.org/10.1029/2012GL051996, 2012.

Sharman, R. D., and Pearson, J. M: Prediction of energy dissipation rates for aviation turbulence. Part I: Forecasting nonconvective turbulence. J. Appl. Meteorol. Climatol, 56(2), 317–337, https://doi.org/10.1175/JAMC-D-16-0205.1, 2017.

Song, J., Z.-H., Wang, and Wang, C.: The regional impact of urban heat mitigation

设置了格式: 字体颜色: 自动设置

设置了格式: 字体颜色: 自动设置

设置了格式: 字体颜色: 自动设置

设置了格式: 字体颜色: 自动设置

strategies on planetary boundary layer dynamics over a semiarid city, J. Geophys. Res. Atmos., 123(12), 6410–6422, https://doi.org/10.1029/2018JD028302, 2018.

Sunilkumar, S. V., Muhsin, M., Parameswaran, K., Venkat Ratnam, M., Ramkumar, G., Rajeev, K., Krishna Murthy, B. V., Sambhu Namboodiri, K. V., Subrahmanyam, K. V., Kishore Kumar, K., and Shankar Das, S.: Characteristics of turbulence in the troposphere and lower stratosphere over the Indian Peninsula, J. Atmos. Sol.-Terr. Phys., 133, 36–53, https://doi.org/10.1016/j.jastp.2015.07.015, 2015.

~~Sun, J., C. J., Nappo, L., Mahrt, D., Belušic, B., Grisogono, D. R., Stauffer, et al.: Review of wave-turbulence interactions in the stable atmospheric boundary layer, Rev. Geophys., 53, 956–993, https://doi.org/10.1002/2015RG000487, 2015.~~

Wang, L., and Geller, M. A.: Morphology of gravity-wave energy as observed from 4 years (1998–2001) of high vertical resolution U.S. radiosonde data, J. Geophys. Res. Atmos., 108(D16), 4489, https://doi.org/10.1029/2002JD002786, 2003.

Wang, L., Geller, M. A., and Alexander, M. J.: Spatial and Temporal Variations of Gravity Wave Parameters, Part I: Intrinsic Frequency, Wavelength, and Vertical Propagation Direction, J. Atmos. Sci., 62, 125–142, https://doi.org/10.1175/JAS-3364.1, 2005

Williams, P. D., and Joshi, M. M.: Intensification of winter transatlantic aviation turbulence in response to climate change. Nat. Clim. Chang., 3(7), 644–648, https://doi.org/10.1038/nclimate1866, 2013.

Xia, P., Y., Shan, S., Ye, and Jiang, W.: Identification of Tropopause Height with Atmospheric Refractivity, J. Atmos. Sci., 78(1), 3–16 https://doi.org/10.1175/JAS-D-20-0009.1, 2021.

Zhang, J., S. D., Zhang, C. M., Huang, K. M., Huang, Y., Gong, Q., Gan, and Zhang, Y. H.: Latitudinal and topographical variabilities of free atmospheric turbulence from high-resolution radiosonde data sets, J. Geophys. Res. Atmos., 124, 4283–4298. https://doi.org/10.1029/2018JD029982, 2019.

设置了格式: 无下划线

设置了格式: 字体颜色: 自动设置

设置了格式: 字体颜色: 自动设置

设置了格式: 字体颜色: 自动设置

设置了格式: 字体颜色: 自动设置

设置了格式: 字体颜色: 自动设置

设置了格式: 字体颜色: 自动设置

设置了格式: 字体颜色: 自动设置

Zhang, J., J., Guo, H., Xue, S., Zhang, K., Huang, W. Dong, et al.: Tropospheric gravity waves as observed by the high-resolution China radiosonde network and their potential sources, J. Geophys. Res. Atmos., 127, e2022JD037174, https://doi.org/10.1029/2022JD037174, 2022.

Zhang, J., J., Guo, S., Zhang, and Shao, J.: Inertia-gravity wave energy and instability drive turbulence: Evidence from a near-global high-resolution radiosonde dataset, Clim. Dyn., 58(11), 2927–2939, https://doi.org/10.1007/s00382-021-06075-2, 2022.

Table 1. Comparisons of mean wind shears between HVRRS and ERA5 reanalysis at heights of 0–2 km ~~a.s.l~~a.s.l. (a), 10–15 km ~~a.s.l~~a.s.l. (b), and 20–25 km ~~a.s.l~~a.s.l. (c).

	Polar (NH)	Midlatitude (NH)	Subtropics (NH)	Tropics	Subtropics (SH)	Midlatitude (SH)	Polar (SH)
(a) Wind shear at 0–2 km ~~a.s.l~~a.s.l. (m/s/km)							
HVRRS	12.67	12.94	12.30	10.57	13.03	14.16	15.01
ERA5	7.45	7.68	7.78	5.4	8.44	9.67	8.42
(b) Wind shear at 10–15 km ~~a.s.l~~a.s.l. (m/s/km)							
HVRRS	13.23	14.71	13.02	9.40	13.28	14.64	13.00
ERA5	4.22	6.13	6.82	5.86	6.86	5.20	3.42
(c) Wind shear at 20–25 km ~~a.s.l~~a.s.l. (m/s/km)							
HVRRS	15.12	15.74	15.41	16.76	16.69	16.12	17.15
ERA5	2.87	3.52	4.06	5.27	3.99	3.36	2.92

带格式的: 缩进: 左侧: 0 厘米, 首行缩进: 0 厘米

Table 2. The occurrence rate of low *Ri* at 0.8–1.3 km a.s.l. (a), 2.2–3.2 km a.s.l. (b), 6–15 km a.s.l. (c), and 20–21 km a.s.l. (d). The critical *Ri* (*Rit*) is 1/4 for radiosonde, and it increases from 1/4 to 2 for ERA5 reanalysis. Note that HVRRS data were vertically resampled to 100-m, 200-m, 300-m, and 400-m at these four height intervals to match with the ERA5 reanalysis. In addition, the moving average number in Eq.(1) is 0. RS stands for radiosonde.

设置了格式: 字体: 倾斜

设置了格式: 字体: 倾斜

设置了格式: 字体: 倾斜

	Polar (NH)	Midlatitude (NH)	Subtropics (NH)	Tropics	Subtropics (SH)	Midlatitude (SH)	Polar (SH)
(a) Frequency of low *Ri* at 0.8–1.3 km a.s.l. (%) / Vertical resolution of RS is 100-m							
RS, *Rit*=1/4	15.20	24.25	22.86	13.92	22.09	22.43	20.77
ERA5, *Rit*=1/4	2.55	8.88	6.37	2.19	6.80	4.47	2.94
ERA5, *Rit*=0.5	3.77	12.06	9.63	3.65	11.91	7.95	7.22
ERA5, *Rit*=1	8.54	21.22	20.48	8.27	25.45	18.21	15.78
ERA5, *Rit*=1.5	14.18	29.62	30.44	12.88	36.07	27.97	23.22
ERA5, *Rit*=2	19.44	36.58	38.32	17.20	43.72	36.00	29.68
(b) Frequency of low *Ri* at 2.2–3.2 km a.s.l. (%) / Vertical resolution of RS is 200-m							
RS, *Rit*=1/4	3.04	6.22	9.00	5.67	9.71	4.29	3.98
ERA5, *Rit*=1/4	0.24	0.60	1.00	1.30	2.26	0.26	0.1
ERA5, *Rit*=0.5	0.37	1.03	1.96	2.10	4.22	0.50	0.18
ERA5, *Rit*=1	1.16	3.26	6.35	5.20	10.00	2.20	0.91
ERA5, *Rit*=1.5	2.77	6.75	12.20	9.00	16.31	5.60	2.68
ERA5, *Rit*=2	5.02	10.85	18.05	13.03	22.45	9.84	5.10
(c) Frequency of low *Ri* at 6–15 km a.s.l. (%) / Vertical resolution of RS is 300-m							
RS, *Rit*=1/4	0.76	2.24	3.91	5.98	4.46	1.98	0.59
ERA5, *Rit*=1/4	0.10	0.38	0.54	1.46	0.56	0.24	0.05
ERA5, *Rit*=0.5	0.32	1.16	1.95	4.36	2.10	0.93	0.15
ERA5, *Rit*=1	1.37	4.33	7.72	13.14	8.89	3.51	0.61
ERA5, *Rit*=1.5	2.93	8.31	14.54	21.78	17.05	6.76	1.38
ERA5, *Rit*=2	4.70	12.35	20.91	29.28	24.55	10.02	2.32
(d) Frequency of low *Ri* at 20–21 km a.s.l. (%) / Vertical resolution of RS is 400-m							
RS, *Rit*=1/4	0.03	0.07	0.13	0.04	0.04	0.10	0.07
ERA5, *Rit*=1/4	0.01	0.02	0.01	0.02	0.02	0.03	0.04
ERA5, *Rit*=0.5	0.02	0.03	0.01	0.02	0.03	0.04	0.04
ERA5, *Rit*=1	0.03	0.05	0.04	0.05	0.05	0.08	0.04
ERA5, *Rit*=1.5	0.04	0.11	0.13	0.19	0.09	0.17	0.04

设置了格式: 字体: 11 磅
设置了格式: 字体: 11 磅, 倾斜
设置了格式: 字体: 11 磅
设置了格式: 字体: (默认) Times New Roman, 11 磅
设置了格式: 字体: (默认) Times New Roman, 11 磅
设置了格式: 字体: 11 磅
设置了格式: 字体: (默认) Times New Roman, 11 磅
设置了格式: 字体: 11 磅
设置了格式: 字体: (默认) Times New Roman, 11 磅
设置了格式: 字体: 11 磅
设置了格式: 字体: (默认) Times New Roman, 11 磅
设置了格式: 字体: (默认) Times New Roman, 小四
带格式的: 列表段落, 编号 + 级别: 1 + 编号样式: a, b, c, … + 起始编号: 1 + 对齐方式: 左侧 + 对齐位置: 0 厘米 + 缩进位置: 0.63 厘米
设置了格式: 字体: 倾斜
带格式的: 居中
带格式的: 居中
带格式的: 居中
带格式的: 居中
带格式的: 居中
设置了格式: 字体: (默认) Times New Roman, 小四
带格式的: 列表段落, 编号 + 级别: 1 + 编号样式: a, b, c, … + 起始编号: 1 + 对齐方式: 左侧 + 对齐位置: 0 厘米 + 缩进位置: 0.63 厘米
带格式的: 两端对齐

ERA5, *Rit*=2	0.05	0.21	0.32	0.55	0.18	0.30	0.05

Table 3. Vertical wind shears at 0.8–1.3 km a.s.l. (a), 2.2–3.2 km a.s.l. (b), 6–15 km

带格式的: 行距: 1.5 倍行距

带格式的: 行距: 1.5 倍行距

设置了格式: 字体: 加粗

带格式的: 定义网格后不调整右缩进, 不调整西文与中文之间的空格, 不调整中文和数字之间的空格

a.s.l. (c), and 20–21 km a.s.l. (d). Note that HVRRS data was vertically resampled to 100-m, 200-m, 300-m, and 400-m at these four height intervals to match with the ERA5 reanalysis. RS stands for radiosonde.

	Polar (NH)	Midlatitude (NH)	Subtropics (NH)	Tropics	Subtropics (SH)	Midlatitude (SH)	Polar (SH)
(a) Wind shear at 0.8–1.3 km a.s.l. (m/s/km) / Vertical resolution of RS is 100-m							
RS	12.50	13.63	11.80	9.83	13.54	13.06	13.85
ERA5	5.43	5.92	6.47	4.83	7.02	6.71	6.05
(b) Wind shear at 2.2–3.2 km a.s.l. (m/s/km)/ Vertical resolution of RS is 200-m							
RS	8.31	9.09	9.24	9.08	9.45	9.39	10.00
ERA5	3.72	4.47	5.19	4.65	5.41	4.71	4.19
(c) Wind shear at 6–15 km a.s.l. (m/s/km) / Vertical resolution of RS is 300-m							
RS	8.30	9.50	9.41	7.72	9.80	9.38	8.00
ERA5	4.00	5.22	5.84	5.21	6.14	4.76	3.37
(d) Wind shear at 20–21 km a.s.l. (m/s/km) / Vertical resolution of RS is 400-m							
RS	9.02	10.40	11.67	12.56	12.14	10.48	9.80
ERA5	3.00	3.83	4.79	5.59	4.72	3.63	2.98

设置了格式: 字体: (默认) Times New Roman, 小四

设置了格式: 字体: (默认) Times New Roman

设置了格式: 字体: (默认) Times New Roman, 小四

带格式的: 编号 + 级别: 1 + 编号样式: a, b, c, … + 起始编号: 1 + 对齐方式: 左侧 + 对齐位置: 0 厘米 + 缩进位置: 0.63 厘米

设置了格式: 字体: (默认) Times New Roman, 小四

设置了格式: 字体: (默认) Times New Roman

设置了格式: 字体: (默认) Times New Roman, 小四

带格式的: 编号 + 级别: 1 + 编号样式: a, b, c, … + 起始编号: 1 + 对齐方式: 左侧 + 对齐位置: 0 厘米 + 缩进位置: 0.63 厘米

Table ~~4~~2. Similar to Tab.1 but for the occurrence frequency of *Ri<Rit*~~KHI~~. Note that *Rit*~~the occurrence of KHI~~ is indicated by *Ri*<1/4 in radiosonde, but it is identified with ~~*Ri*<~~1 in ERA5 reanalysis.

(a) ~~*OF*(KHI)~~*OF*(*Ri<Rit*) at 0–2 km ~~a.s.l~~a.s.l. (%)							
	Polar (NH)	**Midlatitude (NH)**	**Subtropics (NH)**	**Tropics**	**Subtropics (SH)**	**Midlatitude (SH)**	**Polar (SH)**
HVRRS	9.56	16.10	15.78	13.08	16.98	15.38	13.97
ERA5	26.91	33.85	35.70	37.27	40.56	40.46	26.55
(b) ~~*OF*(KHI)~~*OF*(*Ri<Rit*) at 10–15 km ~~a.s.l~~a.s.l. (%)							
HVRRS	0.53	2.22	5.44	11.22	6.17	1.55	0.62
ERA5	0.44	2.62	6.86	17.03	7.15	1.67	0.28
(c) ~~*OF*(KHI)~~*OF*(*Ri<Rit*) at 20–25 km ~~a.s.l~~a.s.l. (%)							
HVRRS	0.36	0.49	0.43	0.5	0.40	0.67	1.35
ERA5	0.06	0.07	0.04	0.1	0.06	0.06	0.04

设置了格式: 字体: 非倾斜

设置了格式: 字体: 倾斜

设置了格式: 字体: 倾斜

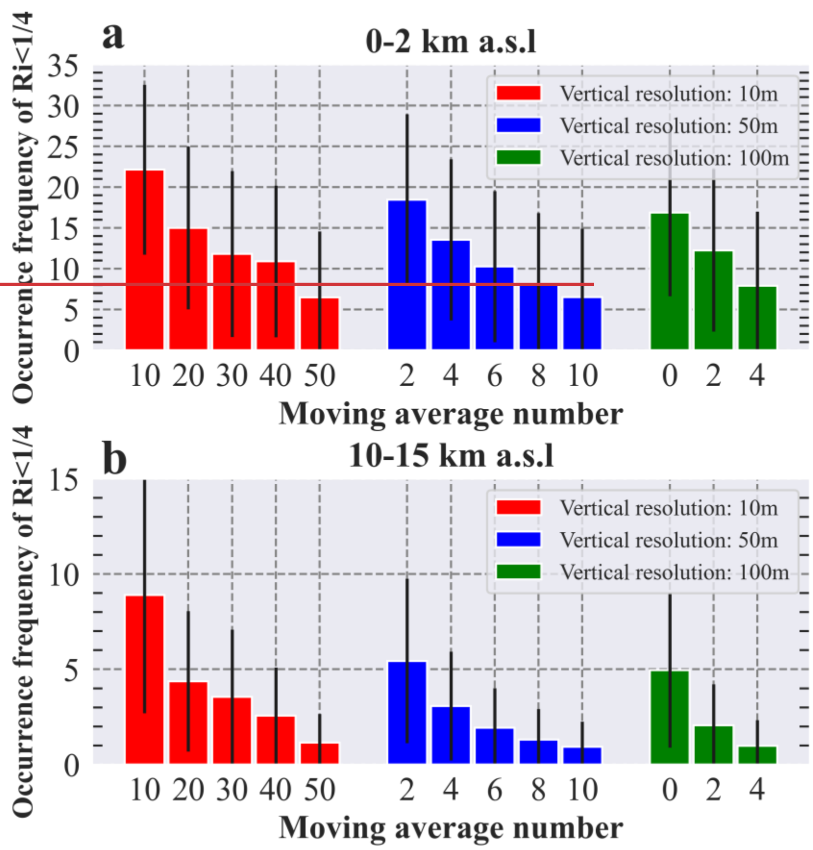
a
0-2 km a.s.l
Vertical resolution: 10m
Vertical resolution: 50m
Vertical resolution: 100m
Occurrence frequency of Ri<1/4
Moving average number
b
10-15 km a.s.l
Vertical resolution: 10m
Vertical resolution: 50m
Vertical resolution: 100m
Occurrence frequency of Ri<1/4
Moving average number

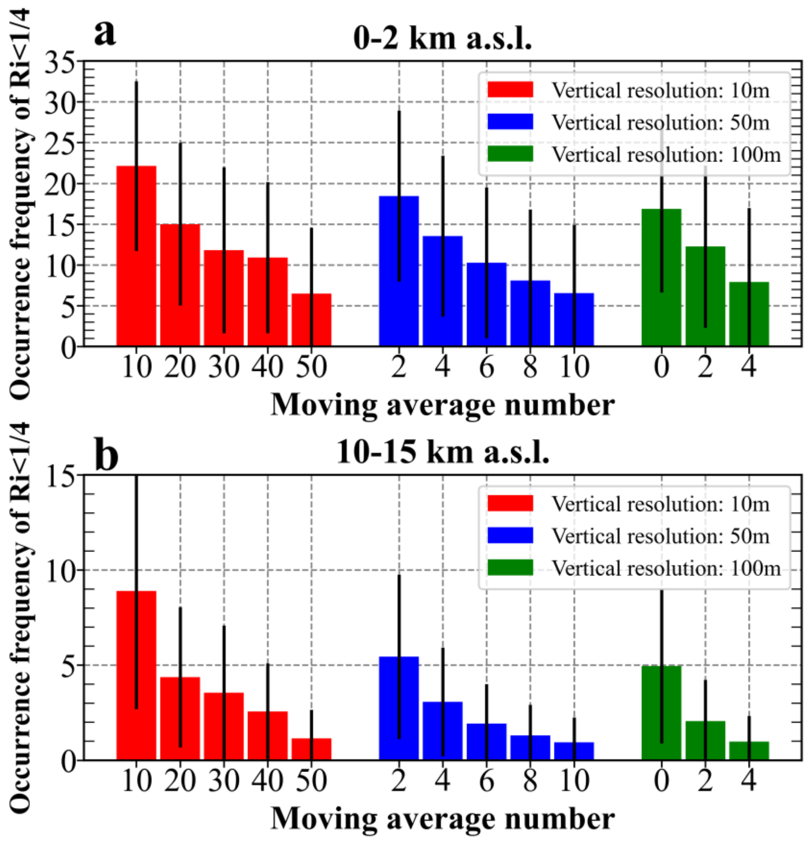

Figure 1. The averaged occurrence frequencies of *Ri*<1/4 at heights of 0–2 km ~~a.s.l~~a.s.l. (a) and 10–15 km ~~a.s.l~~a.s.l. (b), with vertical resolutions ranging 10-m to 100-m and moving point numbers increasing from 0 to 50. The error bars correspond to the standard deviation. The metrics are counted based on all radiosonde profiles during years 2017–2022.

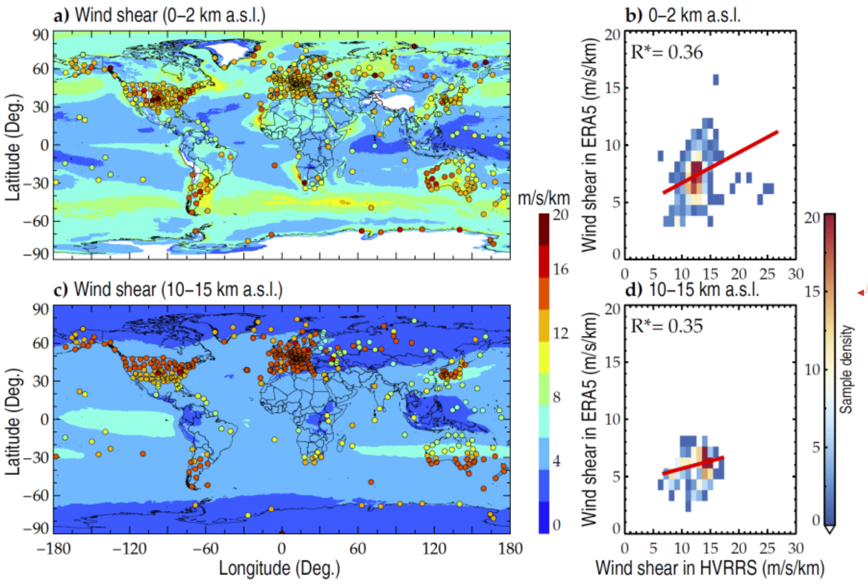

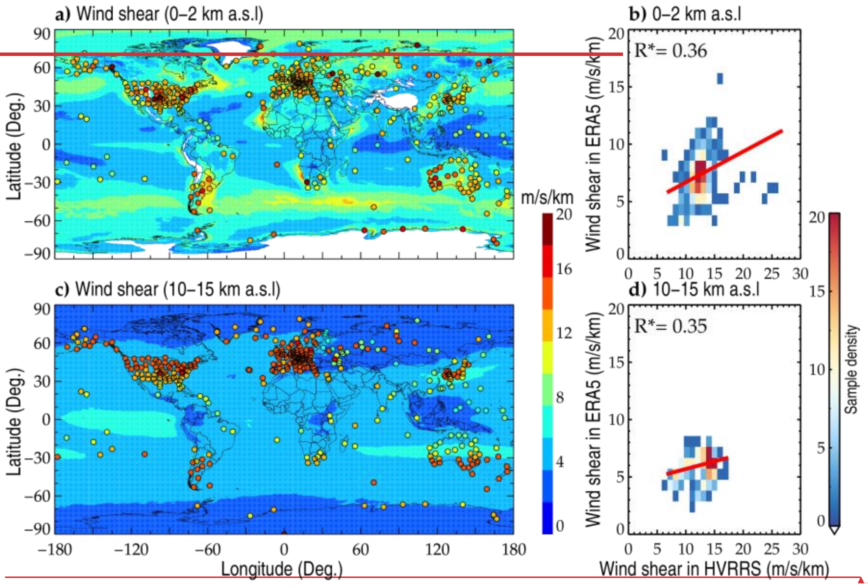

Figure 2. The spatial distribution of mean wind shear in ERA5 reanalysis at heights of 0–2 km a.s.la.s.l. (a) and 10–15 km a.s.la.s.l. (c), where the areas with a near-surface pressure lower than 800 hPa are masked with white. The overlaid colored circles represent the result in HVRRS at the same height levels. Each data point represents a vertically averaged value of the wind shear at one radiosonde station during the whole

带格式的: 左, 行距: 单倍行距, 孤行控制

设置了格式: 字体: (默认) 宋体, (中文) 宋体

study period. Density plots (b, d) show the correlation between wind shears in HVRRS and ERA5 reanalysis. The ERA5 derived wind shears are spatially and temporally collocated with those of HVRRS. In addition, the red lines represent a least-squared linear regression, and the star superscripts indicate that values are statistically significant (p<0.05).

设置了格式: 非突出显示

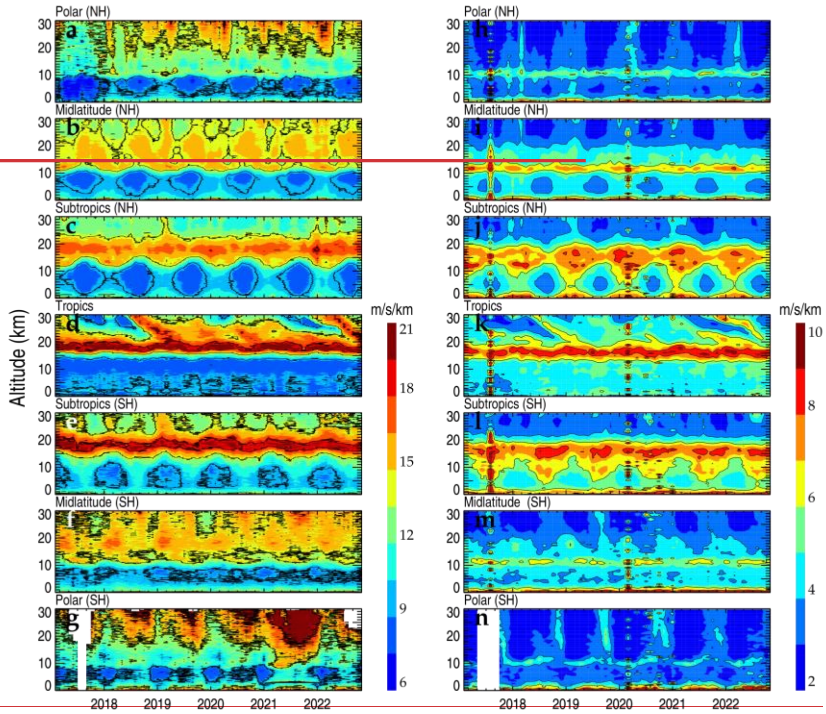

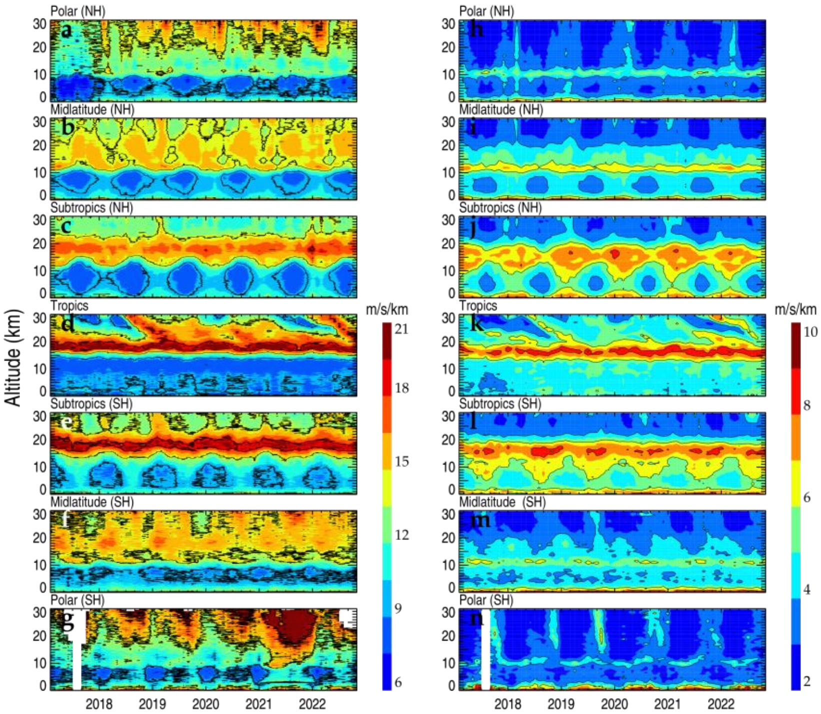

Figure 3. Monthly mean wind shears during years 2017–2022 in HVRRS (a–g) and ERA5 reanalysis (h–n) at different climate zones. The ERA5 derived wind shears are spatially and temporally collocated with those of HVRRS. NH=Northern Hemisphere; SH=Southern Hemisphere.

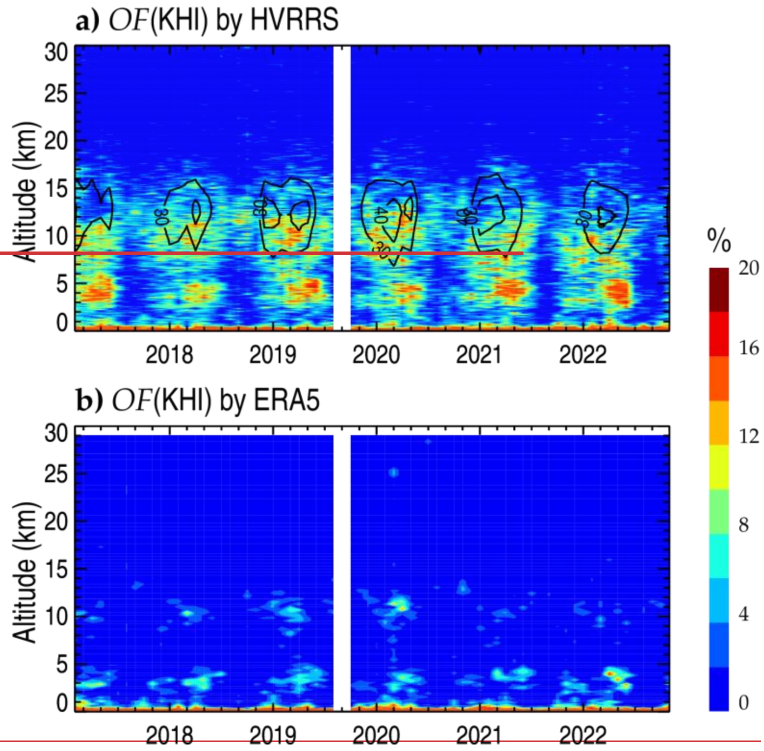
a) OF(KHI) by HVRRS
b) OF(KHI) by ERA5
Altitude (km)
2018
2019
2020
2021
2022
%
20
16
12
8
4
0

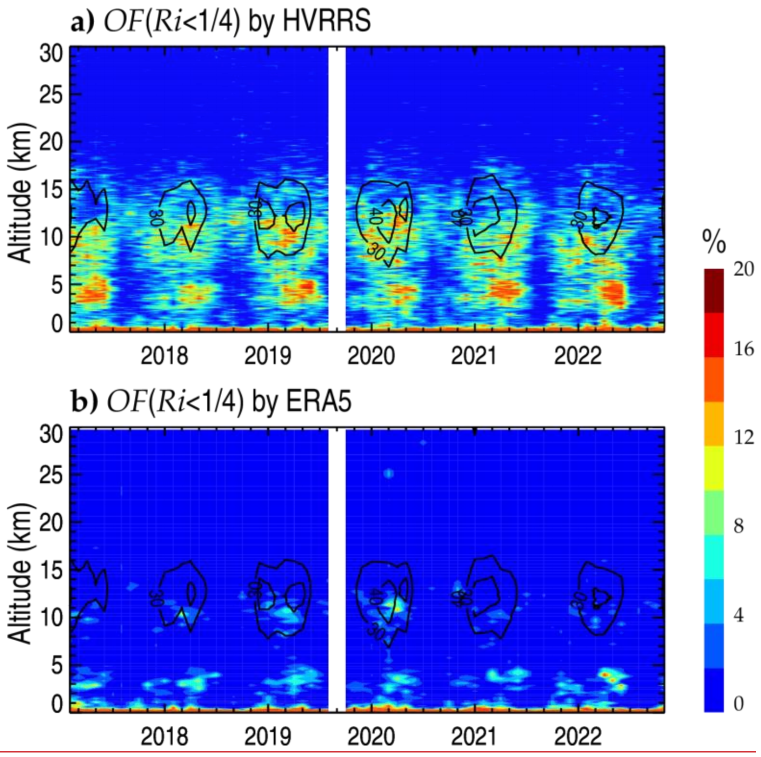

Figure 4. The monthly occurrence frequency of $Ri<1/4$ at Corpus Christi station (27.77° N, −97.5° W) in HVRRS (a) and ERA5 reanalysis (b). Note that the contour curves in (a) and (b) concern the mean horizontal wind speed, and that the ERA5 derived quantities are spatially and temporally collocated with those of HVRRS.

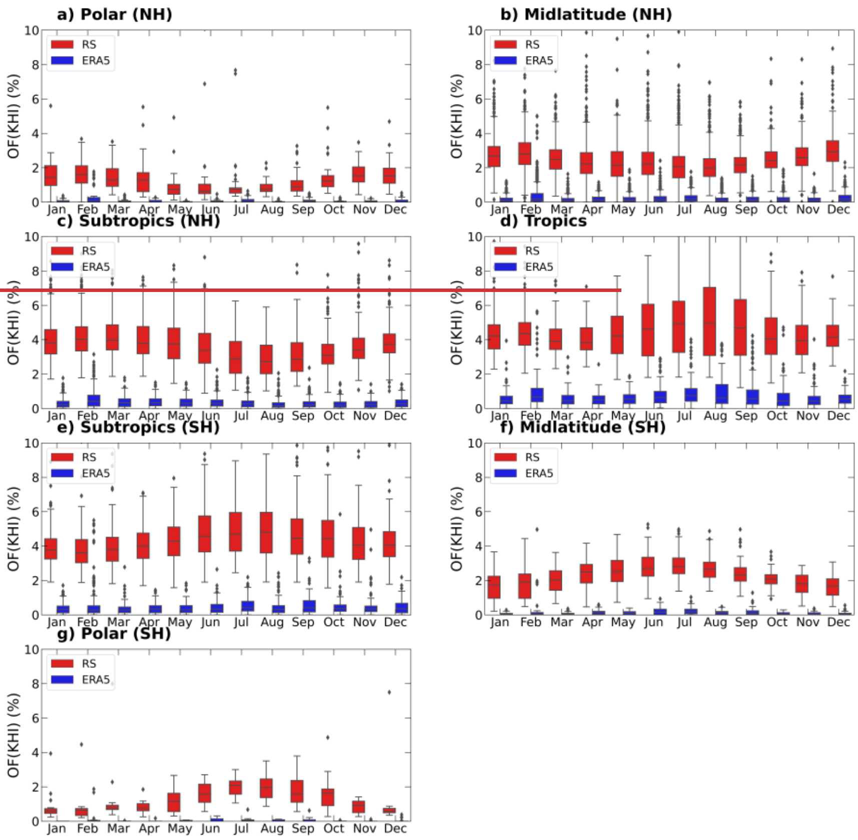
a) Polar (NH)
b) Midlatitude (NH)
c) Subtropics (NH)
d) Tropics
e) Subtropics (SH)
f) Midlatitude (SH)
g) Polar (SH)
RS
ERA5
OF(KHI) (%)
0 2 4 6 8 10
Jan Feb Mar Apr May Jun Jul Aug Sep Oct Nov Dec

带格式的: 两端对齐

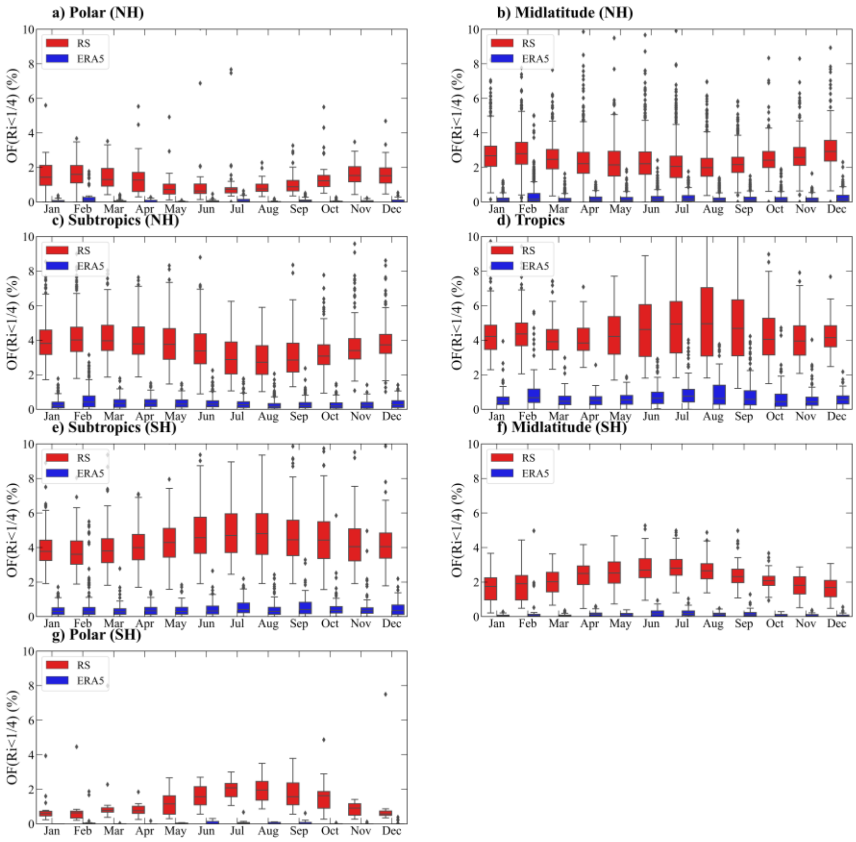

Figure 5. The annual cycles of the occurrence frequency of *Ri*<1/4 in different climate zones at 10–15 km ~~a.s.l~~a.s.l.. The red and blue boxes represent the frequencies in HVRRS and ERA5 reanalysis, respectively. The ERA5 derived *Ri* is spatially and temporally collocated with that of HVRRS. NH, Northern Hemisphere; SH, Southern Hemisphere.

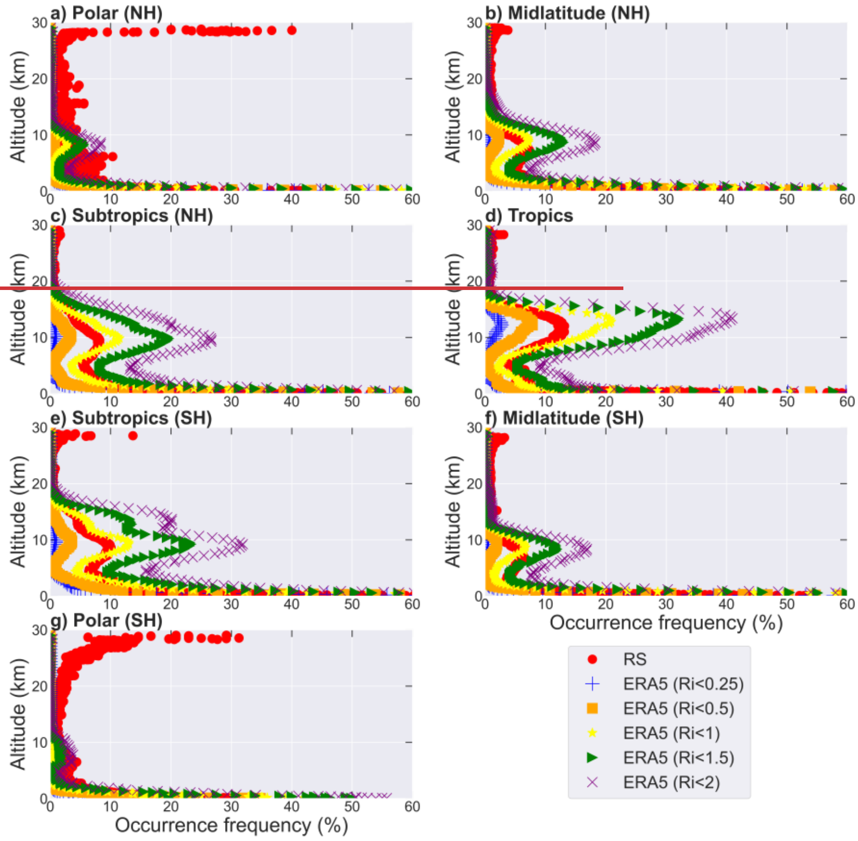
a) Polar (NH)
b) Midlatitude (NH)
c) Subtropics (NH)
d) Tropics
e) Subtropics (SH)
f) Midlatitude (SH)
g) Polar (SH)
Altitude (km)
Occurrence frequency (%)
RS
ERA5 (Ri<0.25)
ERA5 (Ri<0.5)
ERA5 (Ri<1)
ERA5 (Ri<1.5)
ERA5 (Ri<2)

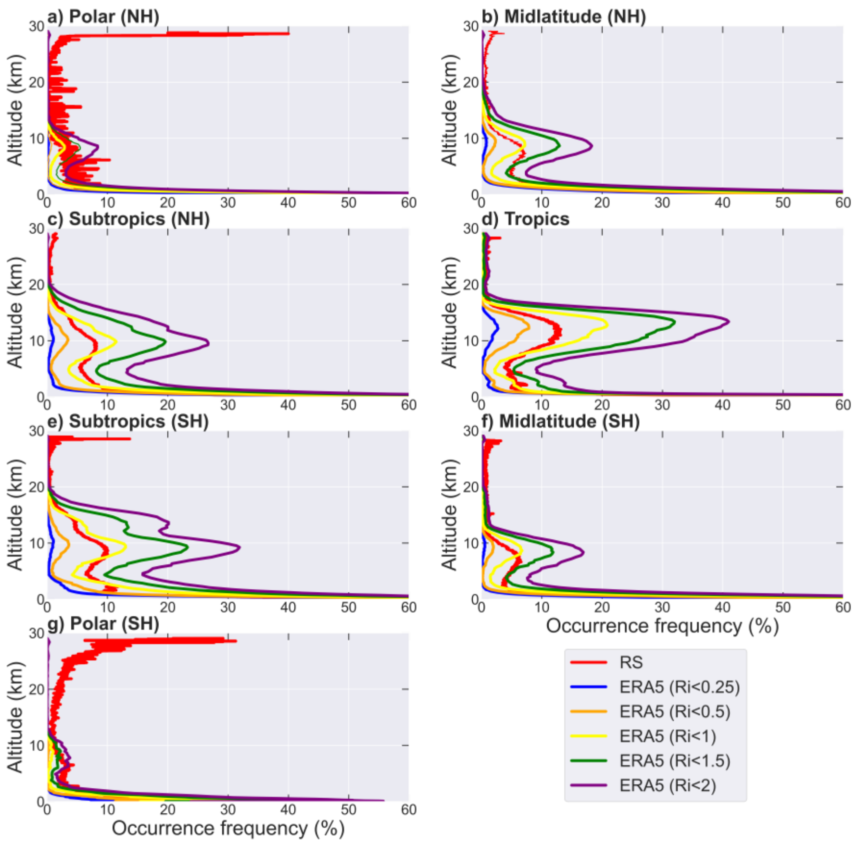

Figure 6. The altitude variation of the occurrence frequency of *Ri* below certain thresholds (0.25, 0.5, 1, 1.5, and 2) in ERA5 reanalysis in various climate zones. The ERA5 derived *Ri* is spatially and temporally collocated with that of HVRRS. The occurrences of *Ri*<1/4 in HVRRS are overlapped with red linesmarked with red dots.

设置了格式: 字体颜色: 自动设置

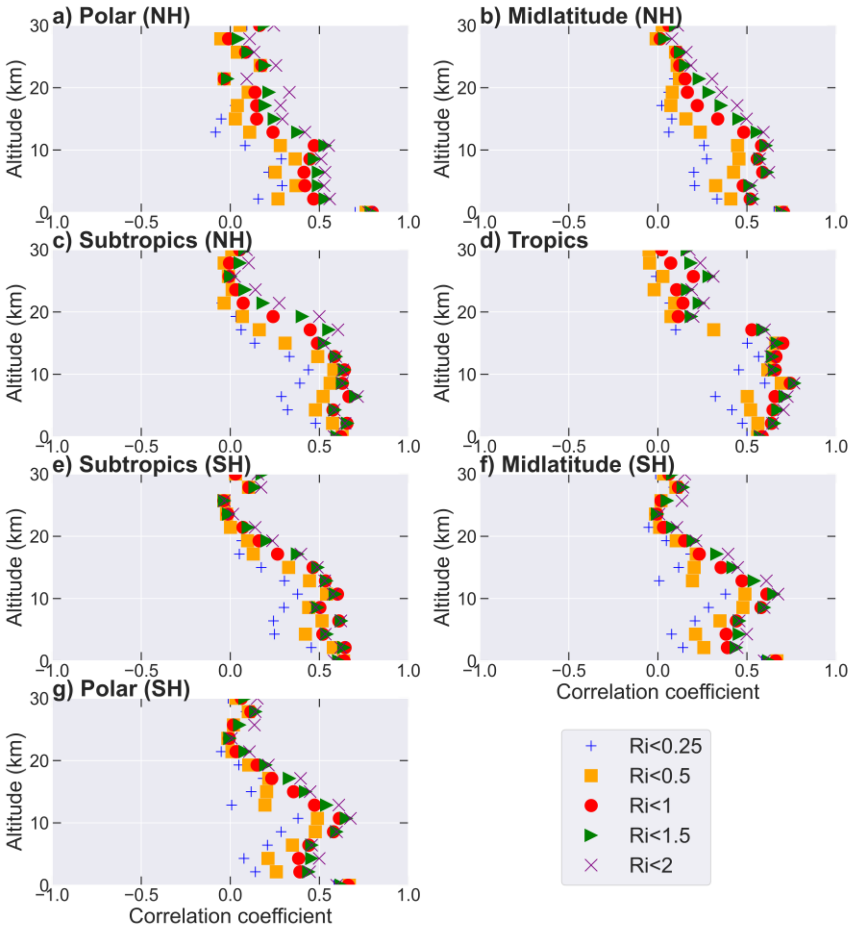

Figure 7. The correlation coefficients between monthly averaged ~~KHI~~ occurrence frequency of *Ri*<1/4 in the HVRRS and the monthly occurrence frequency of *Ri* below certain thresholds (0.25, 0.5, 1, 1.5, and 2) in ERA5 reanalysis. The ERA5 derived *Ri* is spatially and temporally collocated with that of HVRRS. The coefficients in various climate zones are estimated in an increment of 2 km.

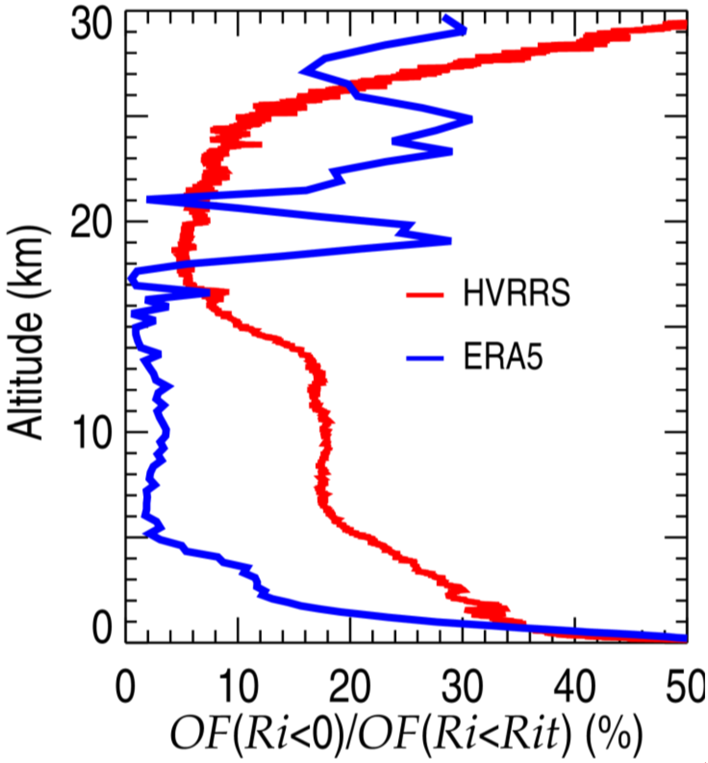

Figure 8. The percentage of *OF*(*Ri*<0) relative to *OF*(*Ri*<*Rit*) in HVRRS (red) and ERA5 reanalysis (blue).

设置了格式: 字体: (默认) 宋体, (中文) 宋体

带格式的: 居中, 行距: 单倍行距, 孤行控制

设置了格式: 字体: 非倾斜

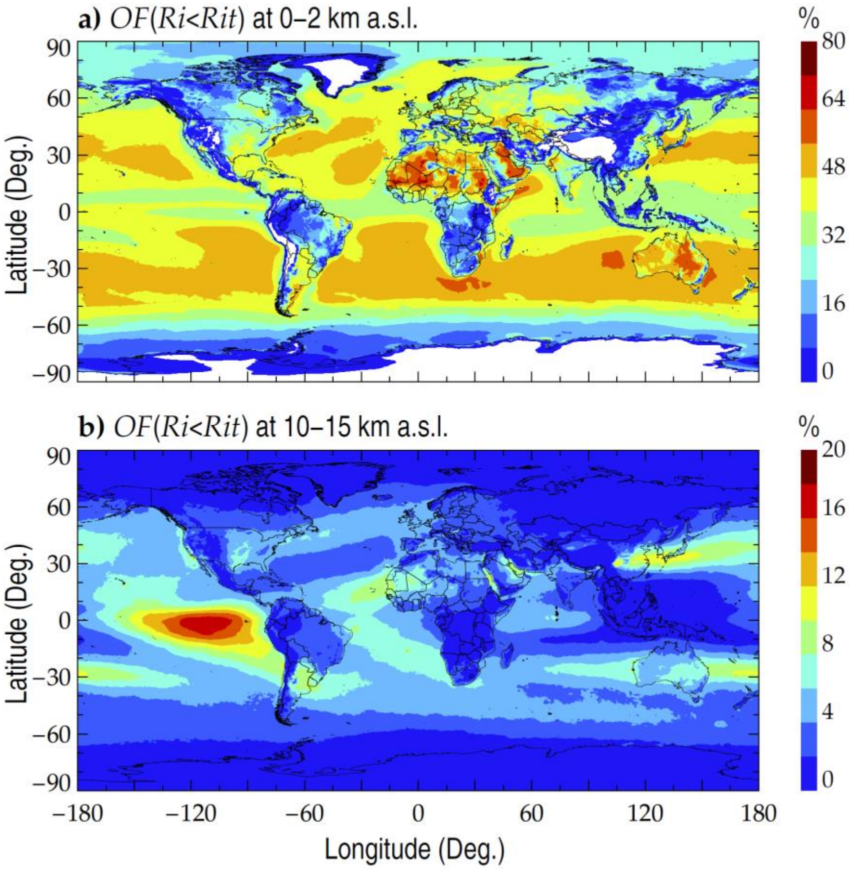

1058

带格式的: 左, 行距: 单倍行距, 孤行控制

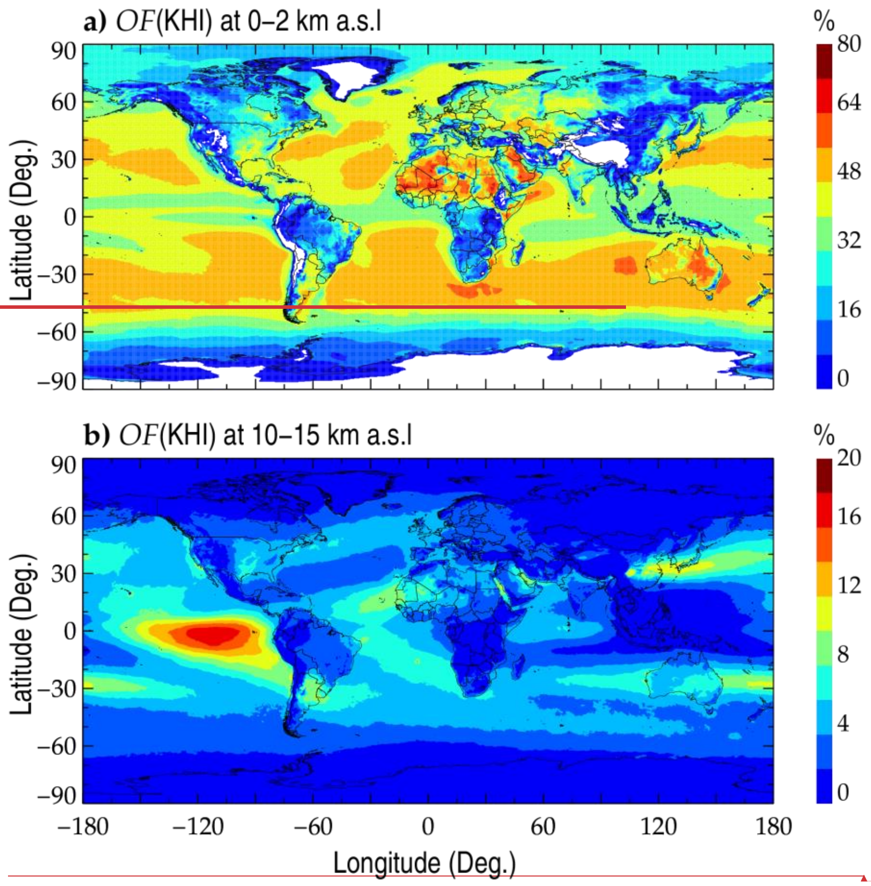

Figure 9~~8~~. The spatial distribution of the mean *OF*(*Ri*<*Rit*) ~~occurrence frequency of KHI~~ in ERA5 reanalysis at 0–2 km ~~a.s.l~~a.s.l. (a) and 10–15 km ~~a.s.l~~a.s.l. (b). Note that *Rit* ~~the threshold value of *Ri*~~ is set to 1.

设置了格式: 字体: (默认) 宋体, (中文) 宋体, 非加粗

1063

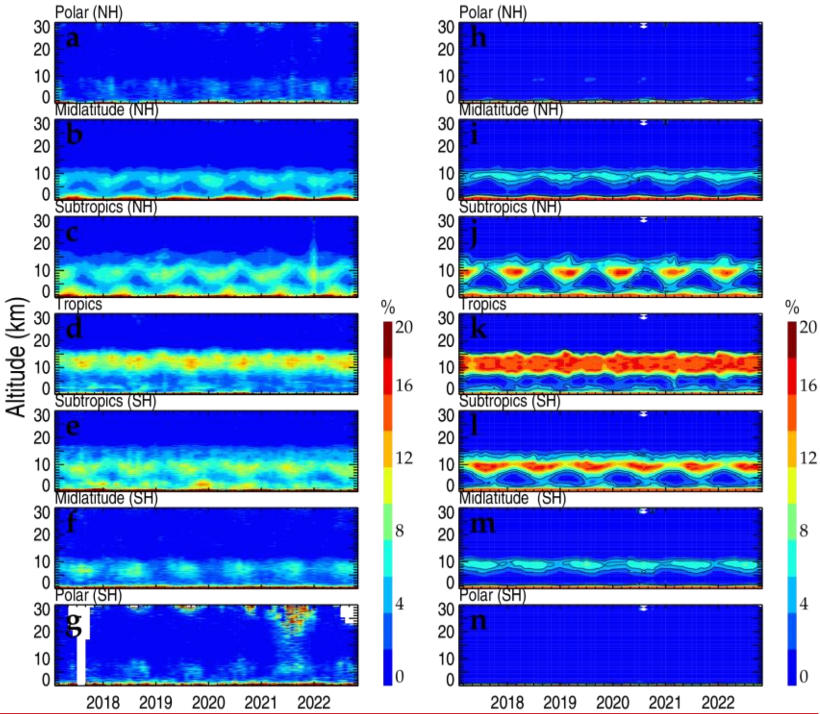
Polar (NH)
Midlatitude (NH)
Subtropics (NH)
Tropics
Subtropics (SH)
Midlatitude (SH)
Polar (SH)
a
b
c
d
e
f
g
h
i
j
k
l
m
n
Altitude (km)
%
2018
2019
2020
2021
2022

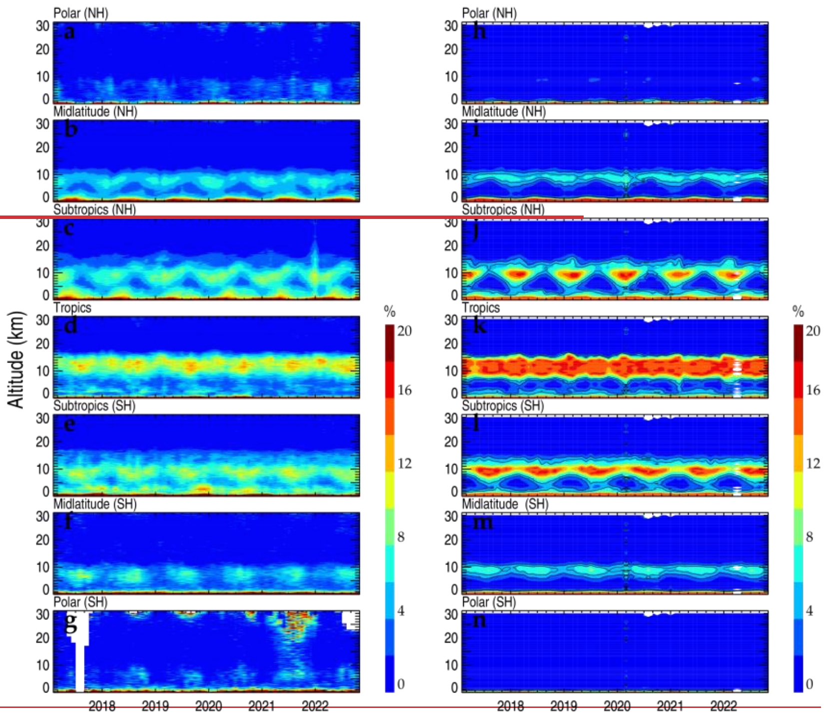

Figure 10~~9~~. The monthly averaged ~~*OF*(KHI)~~*OF*(*Ri*<*Rit*) in the HVRRS (a–g) and ERA5 reanalysis (h–n) in seven climate zones. NH=Northern Hemisphere; SH=Southern Hemisphere.

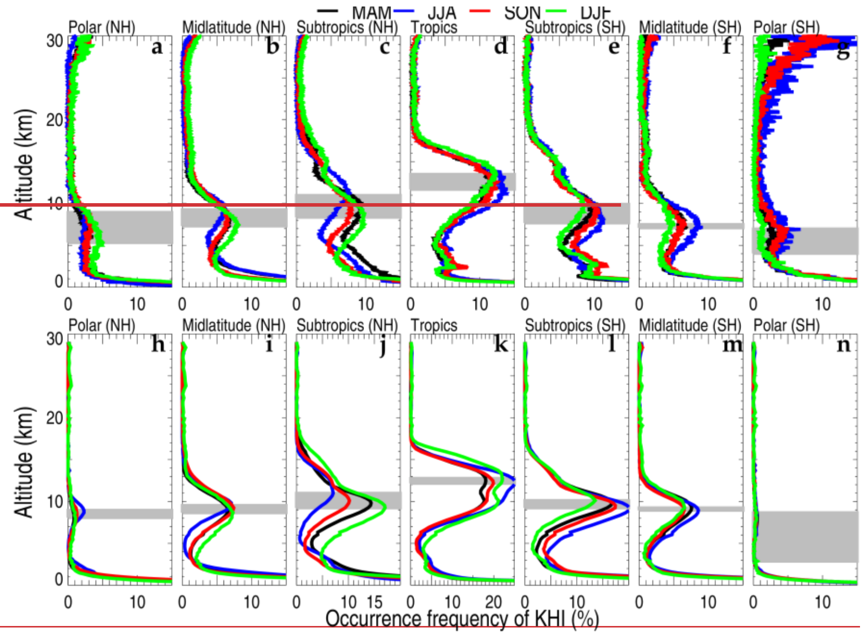

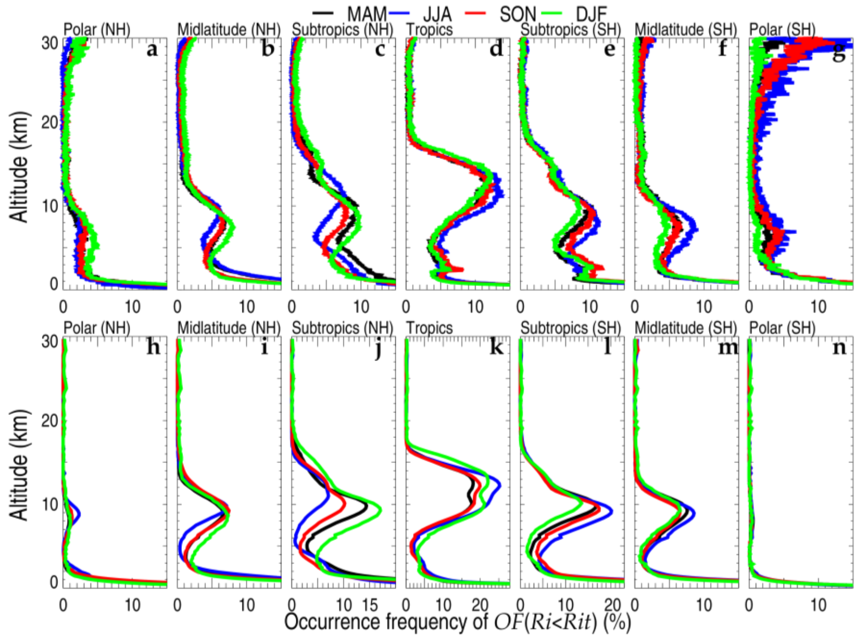

Figure 1~~0~~1. The seasonal averaged ~~*OF*(KHI)~~*OF*(*Ri*<*Rit*) in the HVRRS (a–g) and ERA5 reanalysis (h–m) in seven climate zones. ~~The gray areas indicate the free~~

设置了格式: 字体颜色: 自动设置

~~tropospheric regime with maximal *OF*(KHI) in four seasons.~~ MAM, March–April–May; JJA, June–July–August; SON, September–October–November; DJF, December–January–February. NH=Northern Hemisphere; SH=Southern Hemisphere.

设置了格式: 下划线

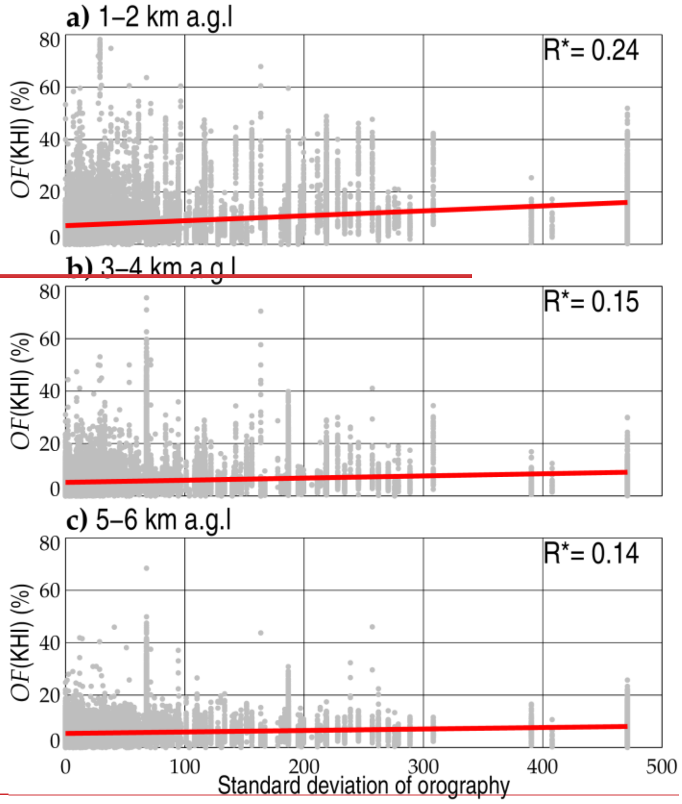
a) 1–2 km a.g.l
R*= 0.24
b) 3–4 km a.g.l
R*= 0.15
c) 5–6 km a.g.l
R*= 0.14
OF(KHI) (%)
0
20
40
60
80
0
100
200
300
400
500
Standard deviation of orography

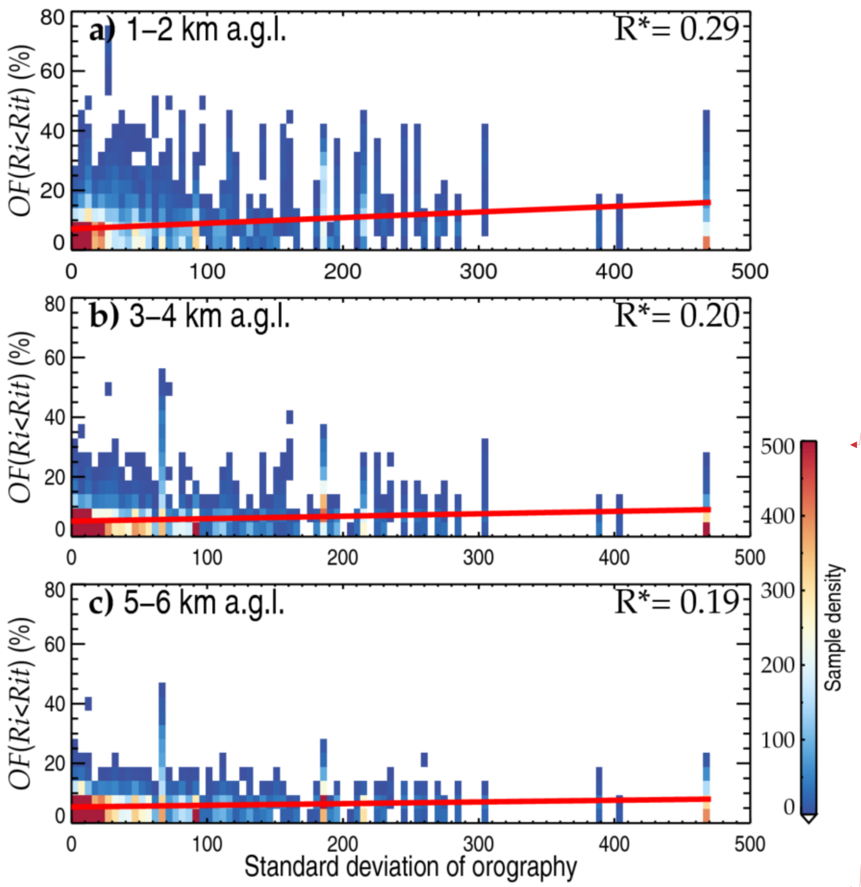

Figure 12~~1~~. The association of HVRRS-determined ~~*OF*(KHI)~~*OF*(*Ri*<*Rit*) with different standard deviations of orography (dimensionless). (a), (b), and (c) are for height ranges of 1–2 km, 3–4 km, and 5–6 km a.g.l., respectively. The correlation coefficients between ~~*OF*(KHI)~~ *OF*(*Ri*<*Rit*) and standard derivation of orography are marked in the top right corner, where the star superscripts indicate that values are statistically significant (p<0.05).

设置了格式: 字体: (默认) 宋体, (中文) 宋体

带格式的: 左, 行距: 单倍行距, 孤行控制

设置了格式: 字体: 倾斜

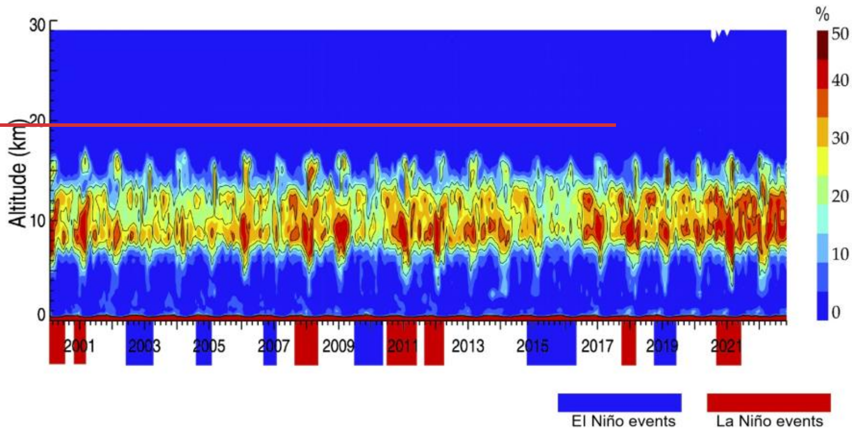

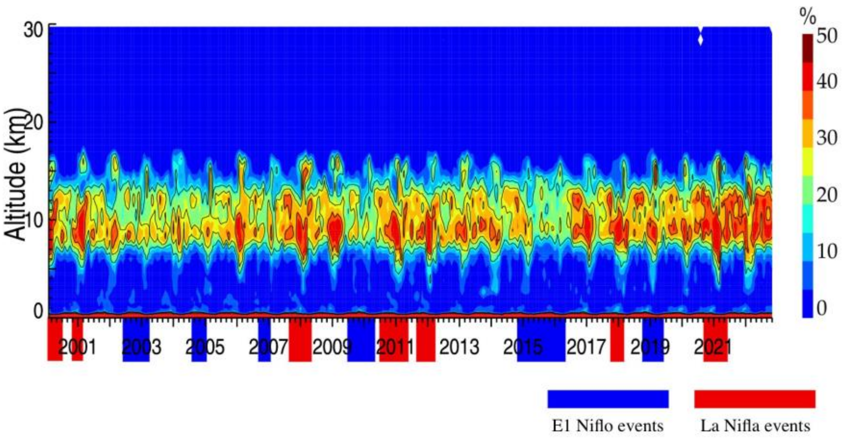

Figure 13~~2~~. The monthly averaged ~~*OF*(KHI)~~*OF(Ri<Rit)* in ERA5 reanalysis over the Niño 3 region (5° N–5° S, 150° W–90° W). The blue and red shadings in time axis indicate the time periods with EI Niño and La Niña~~o~~ events, respectively.

带格式的: 两端对齐, 行距: 1.5 倍行距, 无孤行控制

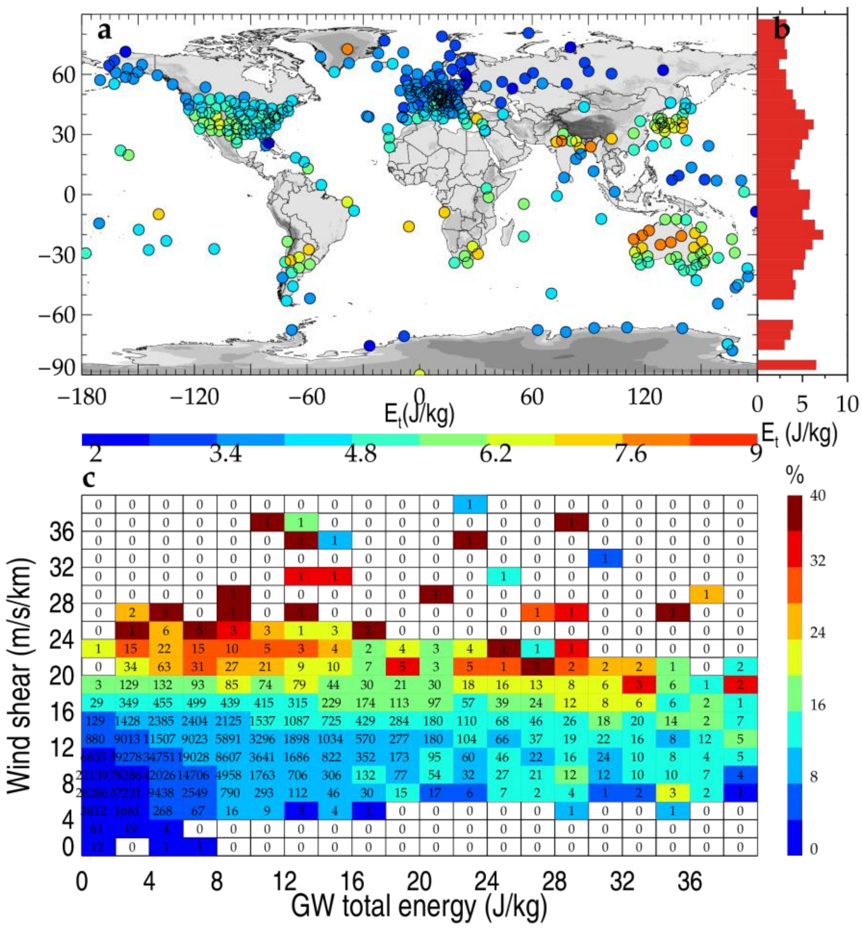

a
b
c
60
30
0
−30
−60
−90
−180
−120
−60
0
60
120
E_t (J/kg)
0
5
10
E_t (J/kg)
2
3.4
4.8
6.2
7.6
9
%
40
32
24
16
8
0
Wind shear (m/s/km)
0
4
8
12
16
20
24
28
32
36
GW total energy (J/kg)

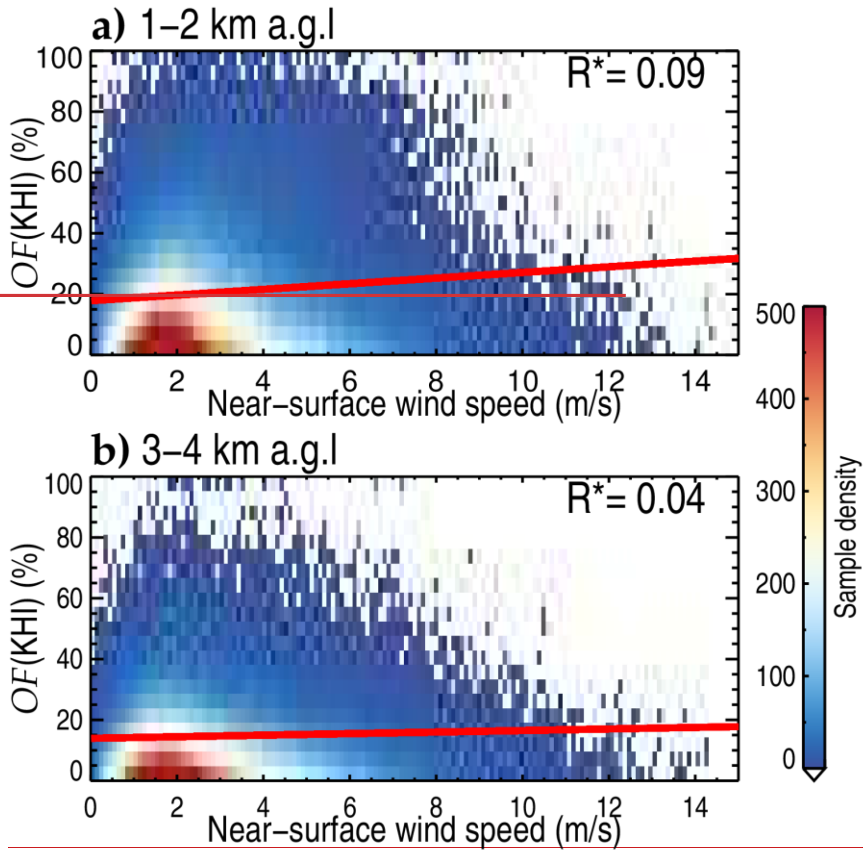

Figure 13. Density plots of HVRRS derived *OF*(KHI) over terrain with standard deviation of orography larger than 50 as a function of near-surface wind speed. The red lines represent a least-squared linear regression. The star superscripts indicate that values are statistically significant ($p<0.05$).

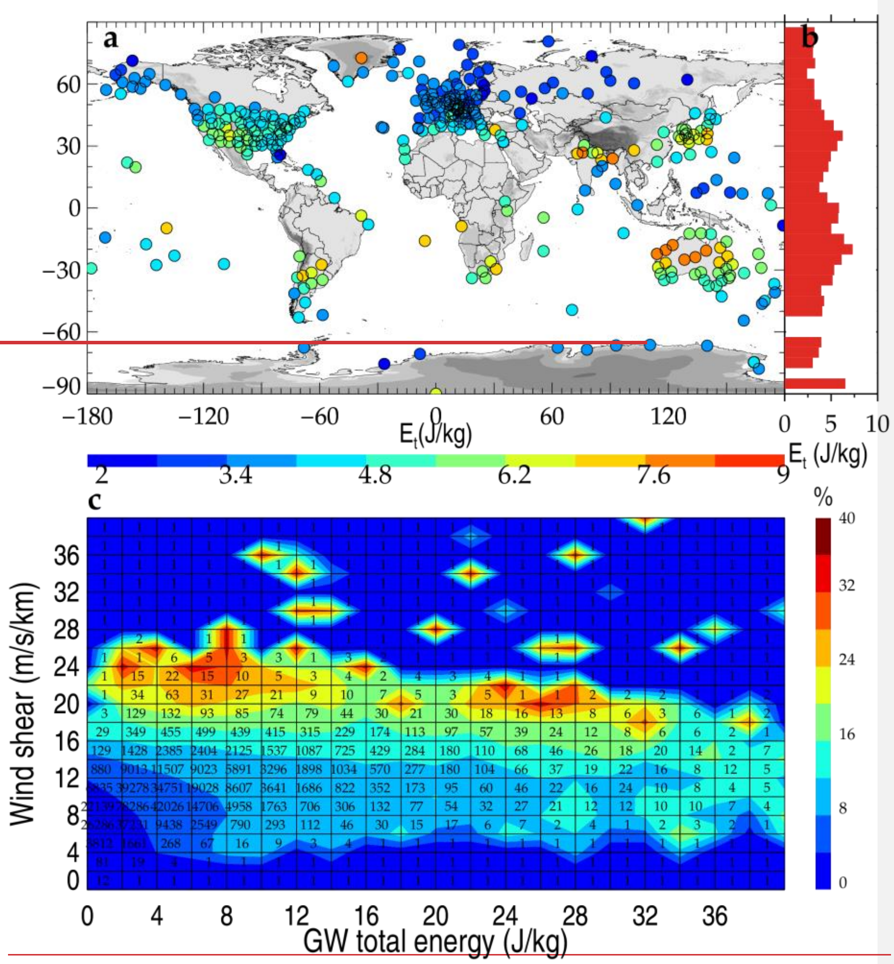

Figure 14. Geographical distribution of mean tropospheric GW total energy obtained from the HVRRS (a). The latitudinal variation of mean energy in a grid cell of 5° latitude (b). The joint distribution of ~~*OF*(KHI)~~*OF*(*Ri*<*Rit*) with GW energy and wind shear (c). The ~~*OF*(KHI)~~*OF*(*Ri*<*Rit*) and wind shear are derived from individual HVRRS profiles and vertically averaged over the tropospheric segment that is used for GW study. The numerical number in (c) indicates the matched profile number in each grid, using a bin size of 2 J/kg along the x axis and 2 m/s/km along the y axis.

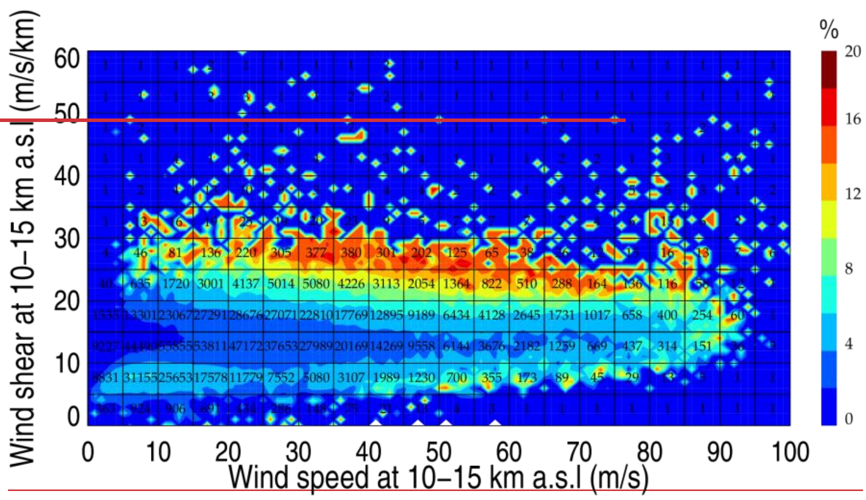

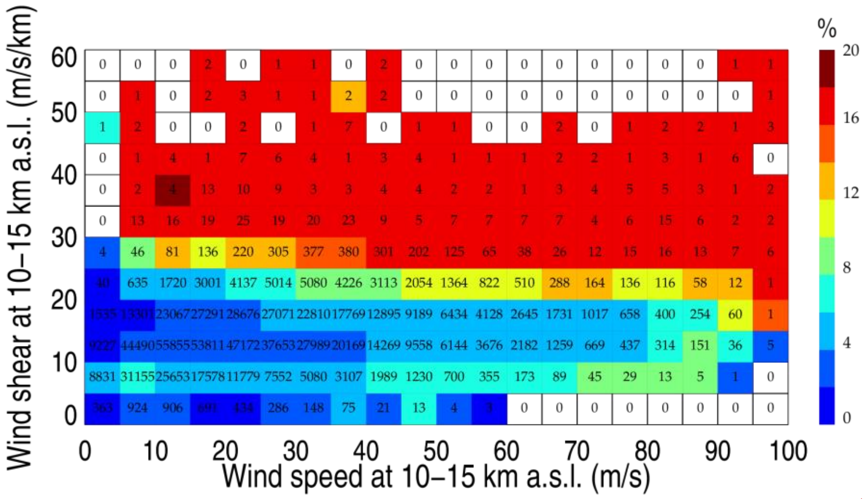

Figure 15. Joint distribution of HVRRS-derived wind speed, wind shear, and ~~*OF*(KHI)~~ *OF*(*Ri*<*Rit*), with a bin size of 5 m/s along the x axis and 5 m/s/km along the y axis. Note that all the relationship is based on the mean result of individual profiles at heights of 10–15 km a.s~~g~~.l.. The number indicates the matched profile number in each grid.

设置了格式: 字体颜色: 自动设置

设置了格式: 字体: (默认) 宋体